Aerodynamic and Gravity Gradient based Attitude Control for CubeSats in the presence of Environmental and Spacecraft Uncertainties

Camilo Riano-Rios[a,*], Runhan Sun[a], Riccardo Bevilacqua[a], Warren E. Dixon[a]

[a] *University of Florida, 939 Sweetwater Dr., Gainesville, FL*

Abstract

In this paper, the problem of controlling the attitude of a CubeSat in low Earth orbit using only the environmental torques is considered. The CubeSat is equipped with a Drag Maneuvering Device (DMD) that enables the spacecraft to modulate its experienced aerodynamic and gravity gradient torques. An adaptive controller is designed to achieve attitude tracking of the spacecraft in the presence of uncertain parameters such as the atmospheric density, drag and lift coefficients, and the time-varying location of the Center of Mass (CoM). The proposed controller also accounts for modeling inaccuracy of the inertia matrix of the spacecraft. A Lyapunov-based analysis is used to prove that the quaternion-based attitude trajectory tracking error is uniformly ultimately bounded. The designed controller is also examined through numerical simulations for a spacecraft with time-varying uncertain drag, lift coefficients and CoM location parameters and the NRLMSISE-00 model for the atmospheric density.

Keywords: Aerodynamic Torque, Gravity Gradient Torque, Atmospheric Density, Drag, Lift, Center of Mass, Adaptive.

---

[*] Corresponding author
Email address: `crianorios@ufl.edu` (Camilo Riano-Rios)

Preprint submitted to Acta Astronautica *December 12, 2020*

1. Introduction

Missions involving small satellites in Low Earth Orbit (LEO) have become popular with the introduction of the CubeSat standard [1]. The limited volume available in these satellites has increased the need to develop propellant-less strategies for orbit and attitude control, usually exploiting the interaction of the spacecraft with the low density atmosphere [2–6]. The idea of using the drag force for relative orbit maneuvers was first introduced in [7]. Since then, a wide variety of control strategies have been developed using both aerodynamic lift and drag as the only control means [8–11]. To exploit such forces, dedicated surfaces are installed on the spacecraft to increase its area-to-mass ratio, often locating the center of pressure at distances with respect to the Center of Mass (CoM) such that significant torques can be applied. This has led to the design of CubeSats that can alter the aerodynamic torques by actively modulating the length and angle of drag surfaces. Such designs often involve several ultra-lightweight surfaces with two or more degrees of freedom [3, 4] so that the inertia matrix does not change significantly and its time derivative can be neglected in the attitude equations of motion.

The University of Florida ADvanced Autonomous MUltiple Spacecraft laboratory (ADAMUS) has designed the Drag Maneuvering Device (DMD), formerly Drag De-Orbit Device (D3) [12], and has been studying its capabilities for spacecraft controlled re-entry [13, 14], spacecraft relative maneuvering [15, 16] and attitude control [17–19] by using its four dedicated surfaces to modulate the experienced environmental forces and torques on a CubeSat. The design of the DMD provides a CubeSat with four repeatedly extendable/retractable surfaces offset 90 degrees from each other, and with 20 degrees inclination with respect to the anti-ram face of the CubeSat. The DMD has passed through several prototype iterations, and incorporates only one degree of freedom for each surface, which makes it easier to build and less susceptible to failure of moving parts. It is also capable of altering the CubeSat inertia matrix to make use of the aerodynamic and the gravity gradient torques.

Previous work in [19] presented the design of an integral concurrent learning-based control method to provide simultaneous state tracking and on-line estimation of uncertain parameters. These uncertain parameters included the average drag coefficient and atmospheric density, and the time-varying CoM location and inertia matrix were assumed known. However, in real operation, inaccurate knowledge of these two parameters could reduce the performance or even destabilize the system. Controllers that actively change the location of the CoM have been proposed for spacecraft attitude control in [20] using PID, linear quadratic regulator and partial feedback linearization techniques, and the developed control laws computed the location of the CoM so that the desired control torques can be produced. The results in [20] demonstrate how the CoM location can influence the overall performance of the system, making it necessary to account for uncertainties in this parameter. The problem of having uncertainties in the CoM location has been addressed in [21] for unmanned aerial vehicles using an adaptive controller for constant CoM. In [22], adaptive control techniques have been used to develop a propellant-based spacecraft attitude controller that considers time-dependent or input-dependent inertia parameters to account for deployable appendages or mass loss, respectively.

In this paper, the designed controller incorporates uncertainties in the CoM location and time-varying drag and lift coefficients, as well as partial knowledge of the inertia matrix of a DMD-equipped CubeSat. The cost for adding this adaptation capability is that the on-line parameter estimation feature is lost compared to [19]. However, the proposed controller provides improved robustness to uncertainties in parameters that are inaccurate and time-varying. The contribution of this paper is the design of an adaptive controller that exploits environmental torques for spacecraft attitude maneuvers in the presence of uncertainties in the time-varying CoM location, atmospheric density, drag and lift coefficients with guaranteed bounded state tracking through a Lyapunov-based stability analysis.

The remainder of this paper is organized as follows. Section 2 describes the DMD device, and Section 3 presents the spacecraft attitude dynamics. Section

4 describes the control objective and the control development. Section 5 shows the corresponding Lyapunov-based stability analysis. Sections 6 and 7 present the numerical simulation and conclusion, respectively.

2. Drag Maneuvering Device

In this paper, the controller design is based on the DMD developed in [12]. It consists of four repeatedly extendable/retractable 3.7 m long and 0.038 m width surfaces offset 90 deg and inclined 20 deg with respect to the anti-ram face of the spacecraft, as depicted in Figure 1.

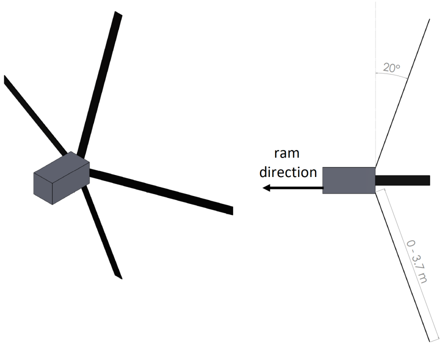

Figure 1: Drag Maneuvering Device schematic.

The surfaces are fabricated from strips of austenitic 316 stainless steel shim stock with 0.0762 mm thickness, weighting approximately 95 g. Given the weight of each boom and their lengths, significant changes in aerodynamic and gravity gradient torques can be created by independently modulating the length of each DMD surface. When the surfaces are fully extended, the DMD provides an increase of the cross-wind surface area up to 0.5 m^2.

3. Attitude Dynamics

3.1. Reference Frames

The Earth-Centered-Inertial (ECI) reference frame is considered the inertial reference frame. The orbital coordinate system is defined as: origin located at the CoM of the spacecraft. The unit vector $\hat{\boldsymbol{o}}_{\mathbf{3}}$ points from the center of the Earth towards the spacecraft CoM, the unit vector $\hat{\boldsymbol{o}}_{\mathbf{2}}$ is aligned with the orbit angular momentum, and the unit vector $\hat{\boldsymbol{o}}_{\mathbf{1}}$ completes a right-hand Cartesian coordinate system. The body coordinate system is defined with the origin located at the CoM of the spacecraft, and the unit vectors $\hat{\boldsymbol{b}}_{\mathbf{1}}$, $\hat{\boldsymbol{b}}_{\mathbf{2}}$ and $\hat{\boldsymbol{b}}_{\mathbf{3}}$ aligned with the longitudinal, lateral, and vertical axes of the spacecraft, respectively, as depicted in Figure 2.

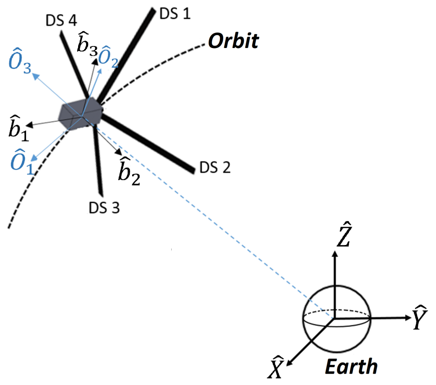

Figure 2: Coordinate systems.

3.2. Equation of Motion

The spacecraft attitude dynamics are given by

$$\dot{J}\boldsymbol{\omega} + J\dot{\boldsymbol{\omega}} + \omega^{\times} J\boldsymbol{\omega} = \boldsymbol{\tau_D} + \boldsymbol{\tau_L} + \boldsymbol{\tau_{GG}} + \boldsymbol{\delta}, \tag{1}$$

where $\boldsymbol{\omega} \in \mathbb{R}^3$ is the angular velocity of the body with respect to the inertial reference frame, $J \in \mathbb{R}^{3\times 3}$ is the inertia matrix of the spacecraft, $\boldsymbol{\tau_{GG}} \in \mathbb{R}^3$ is the gravity gradient torque, and $\boldsymbol{\tau_D}$, $\boldsymbol{\tau_L} \in \mathbb{R}^3$ are the aerodynamic torques due to drag and lift, respectively. The vector $\boldsymbol{\delta} \in \mathbb{R}^3$ denotes disturbances to the system (e.g., magnetic torques). The skew symmetric matrix $a^{\times} \in \mathbb{R}^{3\times 3}$

for a vector $\boldsymbol{a} \triangleq [a_1\ a_2\ a_3]^T \in \mathbb{R}^3$ is defined as

$$a^\times \triangleq \begin{bmatrix} 0 & -a_3 & a_2 \\ a_3 & 0 & -a_1 \\ -a_2 & a_1 & 0 \end{bmatrix}. \tag{2}$$

Remark 1. The design of the DMD considers surfaces made of austenitic stainless steel, which is considered a non-magnetic material [12]. Therefore, the DMD surfaces are not expected to generate magnetic hysteresis torques. An estimate of the maximum remaining magnetic moment of the spacecraft can be computed following the procedure in [23] under the guidelines in [24] for a class II spacecraft.

Assumption 1. The disturbance torque $\boldsymbol{\delta}$ can be upper bounded as $\|\boldsymbol{\delta}\| \leq \zeta_0$, where $\zeta_0 \in \mathbb{R}_{>0}$ is a known bounding constant. □

3.3. Quaternion Representation of the Spacecraft Orientation

The quaternion $\boldsymbol{q} \in \mathbb{R}^4$ represents the rotation of the spacecraft body with respect to an inertial frame, expressed in the body coordinate system as [25]

$$\boldsymbol{q} \triangleq \left[q_0\ \ \boldsymbol{q_v}^T\right]^T, \tag{3}$$

where $q_0 \in \mathbb{R}$ and $\boldsymbol{q_v} = [q_1\ q_2\ q_3]^T \in \mathbb{R}^3$. The quaternion $\boldsymbol{q}$ has the property

$$\boldsymbol{q_v}^T \boldsymbol{q_v} + {q_0}^2 = 1. \tag{4}$$

The rotational kinematics of the spacecraft is defined as

$$\dot{\boldsymbol{q}}_{\boldsymbol{v}} \triangleq \frac{1}{2}\left(q_v^\times + q_0 \mathcal{I}_3\right)\boldsymbol{\omega} \tag{5}$$

$$\dot{q}_0 \triangleq -\frac{1}{2}\boldsymbol{q_v}^T \boldsymbol{\omega}, \tag{6}$$

where $\mathcal{I}_3 \in \mathbb{R}^{3\times 3}$ denotes the identity matrix. To specify a desired time-varying attitude trajectory, we also define a desired quaternion $\boldsymbol{q_d} \in \mathbb{R}^4$ as

$$\boldsymbol{q_d} \triangleq \left[q_{0d}\ \ \boldsymbol{q_{vd}}^T\right]^T, \tag{7}$$

where $q_{0d} \in \mathbb{R}$ and $\boldsymbol{q_{vd}} \in \mathbb{R}^3$. Using (5) and (6), the angular velocity $\boldsymbol{\omega}$ can be expressed in terms of $\boldsymbol{q}$ as

$$\boldsymbol{\omega} = 2\left(q_0 \boldsymbol{\dot{q}_v} - \boldsymbol{q_v} q_0\right) - 2q_v^{\times} \boldsymbol{\dot{q}_v}, \tag{8}$$

and the desired angular velocity of the body $\boldsymbol{\omega_d}$ with respect to the inertial frame can be expressed in the desired body coordinate system as

$$\boldsymbol{\omega_d} = 2\left(q_{0d} \boldsymbol{\dot{q}_{vd}} - \boldsymbol{q_{vd}} q_{0d}\right) - 2{q_{vd}}^{\times} \boldsymbol{\dot{q}_{vd}}. \tag{9}$$

For simplicity, the attitude dynamics will be expressed in the body coordinate system in the subsequent stability analysis. Therefore, it is useful to define the matrices that represent the actual and desired orientation of the body with respect to the inertial frame, which are denoted by $R \in SO(3)$ and $R_d \in SO(3)$, respectively, as [25]

$$R \triangleq \left(q_0^2 - \boldsymbol{q_v}^T \boldsymbol{q_v}\right) \mathcal{I}_3 + 2\boldsymbol{q_v} \boldsymbol{q_v}^T - 2q_0 {q_v}^{\times}, \tag{10}$$

$$R_d \triangleq \left(q_{0d}^2 - \boldsymbol{q_{vd}}^T \boldsymbol{q_{vd}}\right) \mathcal{I}_3 + 2\boldsymbol{q_{vd}} \boldsymbol{q_{vd}}^T - 2q_{0d} {q_{vd}}^{\times}. \tag{11}$$

The error quaternion $\boldsymbol{e} \triangleq [e_0 \; \boldsymbol{e_v}^T]^T \in \mathbb{R}^4$ that represents the mismatch between $\boldsymbol{q}$ and $\boldsymbol{q_d}$ is defined as

$$\boldsymbol{e_v} \triangleq q_{0d} \boldsymbol{q_v} - q_0 \boldsymbol{q_{vd}} + {q_v}^{\times} \boldsymbol{q_{vd}}, \tag{12}$$

$$e_0 \triangleq q_0 q_{0d} + \boldsymbol{q_v}^T \boldsymbol{q_{vd}}, \tag{13}$$

which satisfies the property

$$\boldsymbol{e_v}^T \boldsymbol{e_v} + {e_0}^2 = 1, \tag{14}$$

and obeys the error quaternion kinematics [25]

$$\boldsymbol{\dot{e}_v} = \frac{1}{2}\left({e_v}^{\times} + e_0 \mathcal{I}_3\right) \boldsymbol{\tilde{\omega}}, \tag{15}$$

$$\dot{e}_0 = -\frac{1}{2} \boldsymbol{e_v}^T \boldsymbol{\tilde{\omega}}. \tag{16}$$

In (15) and (16), $\tilde{\boldsymbol{\omega}} \in \mathbb{R}^3$ denotes the error in the angular velocity of the spacecraft

$$\tilde{\boldsymbol{\omega}} \triangleq \boldsymbol{\omega} - \widetilde{R}\boldsymbol{\omega_d}, \tag{17}$$

where $\widetilde{R} \in \mathbb{R}^{3\times 3}$ is the rotation matrix used to express $\boldsymbol{\omega_d}$ in the body coordinate system, and is defined as

$$\widetilde{R} \triangleq RR_d^T = \left({e_0}^2 - \boldsymbol{e_v}^T\boldsymbol{e_v}\right)\mathcal{I}_3 + 2\boldsymbol{e_v}\boldsymbol{e_v}^T - 2e_0{e_v}^{\times}. \tag{18}$$

3.4. Aerodynamic Torques

A spacecraft in LEO experiences drag and lift forces on every surface exposed to the incoming atmosphere particles. In the case of a DMD-equipped CubeSat, the surface areas of the DMD are significantly larger than those of the body so that the latter can be neglected. The drag force $\boldsymbol{F_{D,j}} \in \mathbb{R}^3$ and the lift force $\boldsymbol{F_{L,j}} \in \mathbb{R}^3$ are assumed to act on the geometric center of each DMD surface and can be expressed as

$$\boldsymbol{F_{D,j}} = -\frac{\rho w_b L_j C_{D,j}}{2}\|\boldsymbol{V}_{\perp,j}\|^2\frac{\boldsymbol{V_r}}{\|\boldsymbol{V_r}\|} \tag{19}$$

and

$$\boldsymbol{F_{L,j}} = -\frac{\rho w_b L_j C_{L,j}}{2}\|\boldsymbol{V}_{\perp,j}\|^2\left(\frac{\boldsymbol{V_r}}{\|\boldsymbol{V_r}\|} \times \boldsymbol{n_j} \times \frac{\boldsymbol{V_r}}{\|\boldsymbol{V_r}\|}\right). \tag{20}$$

In (19) and (20), the subscript j indicates the j^{th} DMD surface, $\rho \in \mathbb{R}$ is the atmospheric density, $C_{D,j}$, $C_{L,j}$, w_b, L_j $\in \mathbb{R}$ are drag and lift coefficients, and the width and length of the corresponding DMD surface, respectively. The spacecraft-atmosphere relative velocity vector $\boldsymbol{V_r} \in \mathbb{R}^3$, assuming that the atmosphere co-rotates with the Earth, is defined as

$$\boldsymbol{V_r} \triangleq \dot{\boldsymbol{R}}_{\boldsymbol{c}} - \boldsymbol{\omega}_{\oplus} \times \boldsymbol{R_c}, \tag{21}$$

where $\boldsymbol{\omega}_{\oplus} \in \mathbb{R}^3$ is the angular velocity of the Earth, and $\boldsymbol{R_c}, \dot{\boldsymbol{R}}_{\boldsymbol{c}} \in \mathbb{R}^3$ represent the ECI position and velocity of the spacecraft, respectively. The vector $n_j \in \mathbb{R}^3$

is a unit vector that represents the direction normal to the j^{th} DMD surface and $\boldsymbol{V}_{\perp,j} \triangleq \boldsymbol{V_r}\cdot\boldsymbol{n_j}$.

Remark 2. Density models with different levels of accuracy have been developed throughout the years. The U.S Standard [26] and Harris-Priester [27] models are altitude-based theoretical models that provide values for the atmospheric density based on the spacecraft altitude at a low computational cost. More accurate and complex models, such as the NRLMSISE-00 [28] also incorporate data gathered from real missions to provide atmospheric density values dependent on the date, time, spacecraft position as well as solar and geomagnetic indices. However, more complex density models require significantly higher computational effort and forecasts of solar and geomagnetic activity that are affected by additional uncertainties. Given the multiple sources of uncertainty and approximations in the density models, the error is still significant even with the most accurate ones [29].

The subsequent development is based on the analytical models for drag and lift coefficients presented in [30] that assume flat plates in a free molecular flow as

$$\begin{aligned} C_{D,j} \triangleq {} & \frac{2}{s\sqrt{\pi}}\exp(-s^2\sin^2(\theta_{in})) \\ & + \frac{\sin(\theta_{in})}{s^2}(1+2s^2)\mathrm{erf}(s\sin(\theta_{in})) + \frac{\sqrt{\pi}}{s}\sin^2(\theta_{in})\sqrt{T_{k,out}/T_a} \end{aligned} \tag{22}$$

$$C_{L,j} \triangleq \frac{\cos(\theta_{in})}{s^2}\mathrm{erf}(s\cos(\theta_{in})) + \frac{1}{s}\sqrt{\pi}\cos(\theta_{in})\sin(\theta_{in})\sqrt{T_{k,out}/T_a}, \tag{23}$$

where $\mathrm{erf}(\cdot)$ represents the error function [31], $s \triangleq \|\boldsymbol{V_r}\|\sqrt{m/(2k_BT_a)} \in \mathbb{R}$ is an auxiliary variable, $m \in \mathbb{R}$ is the mass of the spacecraft, $k_B \in \mathbb{R}$ is the Boltzmann constant, $\theta_{in} \in \mathbb{R}$ is the principal rotation angle between $\boldsymbol{V_r}$ and $\boldsymbol{n_j}$, and $T_a \in \mathbb{R}$ is the ambient atmosphere temperature. The kinetic temperature of reflected particles at the surface $T_{k,out} \in \mathbb{R}$ is defined as

$$T_{k,out} \triangleq \frac{m}{3k_B}\|\boldsymbol{V}_r\|^2(1-\alpha) + \alpha T_s, \tag{24}$$

where $T_s \in \mathbb{R}$ is the temperature of the surface, and $\alpha \in \mathbb{R}$ is an accommodation coefficient that represents the influence of the surface material properties.

The torques produced by aerodynamic drag and lift are given by

$$\boldsymbol{\tau_k} \triangleq \sum_{j=1}^{4} R_j{}^{\times} \boldsymbol{F_{k,j}}, \quad k = D, L, \tag{25}$$

where $\boldsymbol{R_j} \triangleq \boldsymbol{r_c} + \boldsymbol{r_j}$, $\boldsymbol{r_c} \triangleq [c_1\ c_2\ c_3]^T \in \mathbb{R}^3$ is the uncertain vector that goes from the spacecraft CoM to the geometric center of the rear face of the CubeSat (O'), and $\boldsymbol{r_j} \in \mathbb{R}^3$ is the vector that goes from O' to the center of pressure of the j^{th} DMD surface. Given the geometry and capabilities of the DMD, the vector $\boldsymbol{r_c}$ also varies with the level of deployment of the drag surfaces.

3.5. Gravity Gradient Torque

The DMD-equipped CubeSat, considered a rigid body in space, experiences a gradient of gravitational force along the body with the greatest attraction on the parts that are closer to the Earth. This gradient produces the so-called Gravity Gradient Torque (GGT) that depends on the attitude and inertia properties. The GGT is given by [32]

$$\boldsymbol{\tau_{GG}} \triangleq \frac{3GM_{\oplus}}{\|\boldsymbol{R}_c\|^5} R_c{}^{\times} J \boldsymbol{R_c}, \tag{26}$$

where $M_{\oplus} \in \mathbb{R}_{>0}$ is the mass of the Earth, and $G \in \mathbb{R}_{>0}$ is the universal gravitational constant.

The GGT can be changed by extending/retracting the DMD surfaces which directly affect the inertia matrix. A simple model to compute the variation of the inertia matrix by assuming DMD surfaces that can be divided as a thick walled cylinder (rolled portion) and a flat plate (deployed portion) [17], is used to propagate the attitude dynamics for the numerical simulation in Section 6.

4. Control Design

4.1. Control Objective

The objective is to design an adaptive controller for the spacecraft attitude to track a given time-varying reference $\boldsymbol{q_d}$ using only the influence of environmental torques on the spacecraft attitude dynamics as described in (1). Uncertainties associated with the average atmospheric density ρ and drag coefficient C_D have been addressed in previous work from the authors in [19]. However, assumptions such as perfect knowledge of the inertia matrix J and the location of the CoM $\boldsymbol{r_c}$ were made to achieve the control objective along with on-line parameter estimation. In this work, at the cost of losing the on-line parameter estimation feature, an augmented vector is proposed to compensate for the uncertainties.

Although analytical models to compute the variation of the inertia matrix can be developed, modeling approximations are inherent and lead to uncertain disturbances. Moreover, modeling deviations in the CoM location will also result in inaccurately computing levels of deployment for the DMD surfaces to produce the torques required by a designed control law.

To achieve the proposed control objective, the subsequent control design will be performed under the following assumptions.

Assumption 2. The spacecraft has the capability of using the computationally light Harris-Priester model [27] to calculate the atmospheric density $\rho_{HP} \in \mathbb{R}_{>0}$ on-board. The real atmospheric density, whose behavior is more complex than what is captured by the Harris-Priester model, is assumed to be approximated by

$$\rho \triangleq B_1 + B_2\ \rho_{HP}, \tag{27}$$

where $B_1,\ B_2 \in \mathbb{R}$ are unknown calibration constants. □

Assumption 3. The spacecraft is capable of approximately computing its time-varying inertia matrix $J_m \in \mathbb{R}^{3\times 3}$, provided an on-board simplified analytical model. The actual inertia matrix J can be expressed as

$$J = J_m + \Delta J, \tag{28}$$

where $\Delta J \in \mathbb{R}^{3\times 3}$ is the mismatch between the actual and modeled inertia matrix. The inertia mismatch ΔJ, as well as its time derivative $\Delta \dot{J}$, are assumed bounded by known constants. Moreover, since the DMD surfaces are driven by motors with limited velocity, then the rate of change of the inertia matrix $\dot{J}$ can also be bounded by a known constant. ☐

Assumption 4. The desired quaternion $\boldsymbol{q_d}$, desired angular velocity $\boldsymbol{\omega_d}$ and its time derivative $\boldsymbol{\dot{\omega}_d}$ are known and bounded signals such that

$$\|\boldsymbol{q_d}\| \leq \zeta_1, \ \ \|\boldsymbol{\omega_d}\| \leq \zeta_2, \ \ \|\boldsymbol{\dot{\omega}_d}\| \leq \zeta_3, \tag{29}$$

where $\zeta_1, \ \zeta_2, \ \zeta_3 \in \mathbb{R}_{>0}$ are known bounding constants. ☐

Assumption 5. The spacecraft is equipped with an attitude determination system that provides the controller with measurements of the angular velocity $\boldsymbol{\omega}$ and quaternion $\boldsymbol{q}$. ☐

Since the components of $\boldsymbol{e}$ satisfy (14), the attitude control objective can be established as

$$\widetilde{R} \to \mathcal{I}_3 \ \text{ as } \ t \to \infty. \tag{30}$$

Based on (12)-(14), the control objective in (30) can be achieved if

$$\|\boldsymbol{e_v}\| \to 0 \Rightarrow | \ e_0 \ | \to 1. \tag{31}$$

4.2. Control Development

Let the modified state vector $\boldsymbol{r} \in \mathbb{R}^3$ be defined as

$$\boldsymbol{r} \triangleq \tilde{\boldsymbol{\omega}} + \beta \boldsymbol{e_v}, \tag{32}$$

where $\beta \in \mathbb{R}^{3\times 3}$ is a symmetric, positive-definite control gain matrix. Taking the time derivative of $\boldsymbol{r}$ and pre-multiplying by the inertia matrix J yields

$$J\dot{\boldsymbol{r}} = \boldsymbol{\tau_D} + \boldsymbol{\tau_L} + \frac{3GM_{\oplus}}{\|\boldsymbol{R_c}\|^5} {R_c}^{\times} J \boldsymbol{R_c} + \boldsymbol{\delta} - \dot{J}\boldsymbol{\omega} - \omega^{\times} J \boldsymbol{\omega} - J\dot{\widetilde{R}}\boldsymbol{\omega_d} - J\widetilde{R}\boldsymbol{\dot{\omega}_d} + J\beta\boldsymbol{\dot{e}_v}. \tag{33}$$

Using (15), (17), Assumption 3 and the fact that $\dot{\widetilde{R}} = -\omega^{\times}\widetilde{R}$ yields

$$J\dot{\boldsymbol{r}} = \boldsymbol{f} + \widetilde{\boldsymbol{N}} + \boldsymbol{N_B}, \tag{34}$$

where $\boldsymbol{f}, \widetilde{\boldsymbol{N}}, \boldsymbol{N_B} \in \mathbb{R}^3$ are auxiliary variables defined as

$$\begin{aligned} \boldsymbol{f} \triangleq\ & \boldsymbol{\tau_D} + \boldsymbol{\tau_L} + \frac{3GM_{\oplus}}{\|\boldsymbol{R_c}\|^5} R_c{}^{\times} J_m \boldsymbol{R_c} - \dot{J}_m \boldsymbol{\omega} \\ & - \omega^{\times} J_m \boldsymbol{\omega} + J_m \omega^{\times} \widetilde{R} \boldsymbol{\omega_d} - J_m \widetilde{R} \dot{\boldsymbol{\omega}}_{\boldsymbol{d}} + J_m \beta \dot{\boldsymbol{e}}_{\boldsymbol{v}}, \end{aligned} \tag{35}$$

$$\begin{aligned} \widetilde{\boldsymbol{N}} \triangleq\ & -\Delta \dot{J} \tilde{\boldsymbol{\omega}} - \tilde{\omega}^{\times} \Delta J \left(\tilde{\boldsymbol{\omega}} + \widetilde{R} \boldsymbol{\omega_d} \right) - \left(\widetilde{R} \boldsymbol{\omega_d} \right)^{\times} \Delta J \tilde{\boldsymbol{\omega}} \\ & + \Delta J \tilde{\omega}^{\times} \widetilde{R} \boldsymbol{\omega_d} + \frac{1}{2} \Delta J \beta \left(e_v{}^{\times} + e_0 \mathcal{I}_3 \right) \tilde{\boldsymbol{\omega}}, \end{aligned} \tag{36}$$

$$\boldsymbol{N_B} \triangleq -\Delta \dot{J} \widetilde{R} \boldsymbol{\omega_d} - \left(\widetilde{R} \boldsymbol{\omega_d} \right)^{\times} \Delta J \widetilde{R} \boldsymbol{\omega_d} + \frac{3GM_{\oplus}}{\|\boldsymbol{R_c}\|^5} R_c{}^{\times} \Delta J \boldsymbol{R_c} + \boldsymbol{\delta} - \Delta J \widetilde{R} \dot{\boldsymbol{\omega}}_{\boldsymbol{d}}. \tag{37}$$

Since $\tilde{\boldsymbol{\omega}} = \boldsymbol{r} - \beta \boldsymbol{e_v}$, and considering that $\|\boldsymbol{R_c}\|$ can be upper bounded by a known constant. Using Assumptions 3 and 4, $\widetilde{\boldsymbol{N}}$ and $\boldsymbol{N_B}$ can be upper bounded as

$$\|\widetilde{\boldsymbol{N}}\| \leq \sigma \left(\|\boldsymbol{\eta}\| \right) \|\boldsymbol{\eta}\|, \tag{38}$$

$$\|\boldsymbol{N_B}\| \leq \zeta_4, \tag{39}$$

where $\zeta_4 \in \mathbb{R}_{>0}$ is a known bounding constant, $\boldsymbol{\eta} \in \mathbb{R}^6$ is an augmented state vector defined as

$$\boldsymbol{\eta} \triangleq \left[\boldsymbol{e_v}^T \ \boldsymbol{r}^T \right]^T, \tag{40}$$

and $\sigma : \mathbb{R}^6 \rightarrow \mathbb{R}$ is a positive, globally invertible and non-decreasing function.

To include the adaptation capabilities that compensate for the unknown parameters, the term $\boldsymbol{f}$ that contains only measurable states and the modeled inertia matrix J_m, can be linearly parameterized with respect to the unknown parameters. First, consider the contribution of the j^{th} DMD surface to the force due to the aerodynamic drag and lift $\boldsymbol{F_{AT,j}} \in \mathbb{R}^3$ which can be expressed using Assumption 2 as

$$\boldsymbol{F_{AT,j}} \triangleq Y_j \boldsymbol{\Theta_j}, \quad j = 1, 2, 3, 4. \tag{41}$$

In (41) $Y_j \in \mathbb{R}^{3\times 4}$ are measurable regression matrices defined as

$$Y_j \triangleq \\ \left[-\frac{L_j w_b \|\boldsymbol{V_{\perp,j}}\|^2}{2\|\boldsymbol{V_r}\|} \boldsymbol{V_r} \left[1 \;\; \rho_{HP}\right] \;\; -\frac{L_j w_b \|\boldsymbol{V}_{\perp,j}\|^2}{2} \left(\frac{\boldsymbol{V_r}}{\|\boldsymbol{V_r}\|} \times \boldsymbol{n_j} \times \frac{\boldsymbol{V_r}}{\|\boldsymbol{V_r}\|} \right) \left[1 \;\; \rho_{HP}\right] \right] \tag{42}$$

and the vectors $\boldsymbol{\Theta_j} \in \mathbb{R}^4$ are

$$\boldsymbol{\Theta_j} \triangleq \begin{bmatrix} B_1 C_{D,j} & B_2 C_{D,j} & B_1 C_{L,j} & B_2 C_{L,j} \end{bmatrix}^T. \tag{43}$$

Therefore, the total aerodynamic torque $\boldsymbol{\tau_{AT,j}} \in \mathbb{R}^3$ due to the aerodynamic drag and lift in (25) can be rewritten as

$$\boldsymbol{\tau_{AT}} \triangleq \boldsymbol{\tau_D} + \boldsymbol{\tau_L} = {r_c}^{\times} \sum_{j=1}^{4} \left(Y_j \boldsymbol{\Theta_j}\right) + \sum_{j=1}^{4} \left({r_j}^{\times} Y_j \boldsymbol{\Theta_j}\right). \tag{44}$$

In (44), the first term can be expressed as

$$ {r_c}^{\times} \sum_{j=1}^{4} \left(Y_j \boldsymbol{\Theta_j}\right) = \begin{bmatrix} \mathbf{0}_{1\times 16} & Y_r(3) & -Y_r(2) \\ -Y_r(3) & \mathbf{0}_{1\times 16} & Y_r(1) \\ Y_r(2) & -Y_r(1) & \mathbf{0}_{1\times 16} \end{bmatrix} \begin{bmatrix} \boldsymbol{\Theta_r} c_1 \\ \boldsymbol{\Theta_r} c_2 \\ \boldsymbol{\Theta_r} c_3 \end{bmatrix}, \tag{45}$$

where $Y_r \in \mathbb{R}^{3\times 16}$ is a measurable regression matrix defined as

$$Y_r \triangleq \begin{bmatrix} Y_1 & Y_2 & Y_3 & Y_4 \end{bmatrix}, \tag{46}$$

and $Y_r(k)$ denotes the k^{th} row of Y_r. Similarly, the vector of uncertain parameters $\boldsymbol{\Theta_r} \in \mathbb{R}^{16}$ is defined as

$$\boldsymbol{\Theta_r} \triangleq \begin{bmatrix} {\boldsymbol{\Theta_1}}^T \; {\boldsymbol{\Theta_2}}^T \; {\boldsymbol{\Theta_3}}^T \; {\boldsymbol{\Theta_4}}^T \end{bmatrix}^T. \tag{47}$$

The second term in (44) can be expressed as

$$\sum_{j=1}^{4}\left(r_j{}^{\times}Y_j\boldsymbol{\Theta_j}\right)=\sum_{j=1}^{4}\left(\begin{bmatrix}Y_j(3)r_{j,2}-Y_j(2)r_{j,3}\\ Y_j(1)r_{j,3}-Y_j(3)r_{j,1}\\ Y_j(2)r_{j,1}-Y_j(1)r_{j,2}\end{bmatrix}\boldsymbol{\Theta_j}\right), \tag{48}$$

where $\boldsymbol{r_j}\triangleq[r_{j,1}\ r_{j,2}\ r_{j,3}]^T$ is the vector defined in (25), and $Y_j(k)$ denotes the k^{th} row of Y_j. Substituting (45) and (48) into (44) yields

$$\boldsymbol{\tau_{AT}}=Y_{AT}\boldsymbol{\Theta_{AT}}, \tag{49}$$

where $Y_{AT}\in\mathbb{R}^{3\times 64}$ is a measurable regression matrix and $\boldsymbol{\Theta_{AT}}\in\mathbb{R}^{64}$ is a vector of uncertain parameters, and are defined as

$$Y_{AT}=$$

$$\begin{bmatrix}\mathbf{0}_{1\times16} & Y_r(3) & -Y_r(2) & Y_1(3)r_{1,2}-Y_1(2)r_{1,3} & \cdots & Y_4(3)r_{4,2}-Y_4(2)r_{4,3}\\ -Y_r(3) & \mathbf{0}_{1\times16} & Y_r(1) & Y_1(1)r_{1,3}-Y_1(3)r_{1,1} & \cdots & Y_4(1)r_{4,3}-Y_4(3)r_{4,1}\\ Y_r(2) & -Y_r(1) & \mathbf{0}_{1\times16} & Y_1(2)r_{1,1}-Y_1(1)r_{1,2} & \cdots & Y_4(2)r_{4,1}-Y_4(1)r_{4,2}\end{bmatrix}, \tag{50}$$

$$\boldsymbol{\Theta_{AT}}=\left[\boldsymbol{\Theta_r}{}^Tc_1\quad \boldsymbol{\Theta_r}{}^Tc_2\quad \boldsymbol{\Theta_r}{}^Tc_3\quad \boldsymbol{\Theta_r}{}^T\right]^T, \tag{51}$$

respectively. Therefore, (35) can be rewritten as

$$\boldsymbol{f}=Y\boldsymbol{\Theta}, \tag{52}$$

where $Y\triangleq\left[Y_{AT}\ \ \frac{3GM_\oplus}{\|\boldsymbol{R_c}\|^5}R_c^\times J_m\boldsymbol{R_c}-\dot{J}_m\boldsymbol{\omega}-\omega^\times J_m\boldsymbol{\omega}+J_m\omega^\times\widetilde{R}\boldsymbol{\omega_d}-J_m\widetilde{R}\dot{\boldsymbol{\omega}}_{\boldsymbol{d}}+J_m\beta\dot{\boldsymbol{e}}_{\boldsymbol{v}}\right]\in\mathbb{R}^{3\times65}$ is the measurable augmented regression matrix, and $\boldsymbol{\Theta}\triangleq\left[\boldsymbol{\Theta_{AT}}{}^T\ 1\right]^T\in\mathbb{R}^{65}$ is the augmented vector of uncertain parameters.

Assumption 6. The time-varying vector of uncertain parameters $\boldsymbol{\Theta}$ and its time derivative, i.e., $\dot{\boldsymbol{\Theta}}$, are bounded by known constants. The bounds for $\boldsymbol{\Theta}$ are given by

$$\underline{\boldsymbol{\Theta}}\leq\boldsymbol{\Theta}\leq\overline{\boldsymbol{\Theta}}, \tag{53}$$

where $\underline{\boldsymbol{\Theta}}, \overline{\boldsymbol{\Theta}} \in \mathbb{R}^{65}$ are constant vectors containing the lower and upper bounds of $\boldsymbol{\Theta}$, respectively. ☐

Define the estimation error $\widetilde{\boldsymbol{\Theta}} \in \mathbb{R}^{65}$ as

$$\widetilde{\boldsymbol{\Theta}} = \boldsymbol{\Theta} - \widehat{\boldsymbol{\Theta}}, \tag{54}$$

where $\widehat{\boldsymbol{\Theta}} \in \mathbb{R}^{65}$ is the estimate of $\boldsymbol{\Theta}$. Using (52) and (54), and adding and subtracting the term $Y\widehat{\boldsymbol{\Theta}}$ to the open-loop error system in (34) yields

$$J\dot{\boldsymbol{r}} = Y\widetilde{\boldsymbol{\Theta}} + Y\widehat{\boldsymbol{\Theta}} + \widetilde{\boldsymbol{N}} + \boldsymbol{N_B}. \tag{55}$$

The regression matrix Y contains measurable states and is influenced by the actual inputs (i.e., the DMD surfaces lengths $L_1,\ L_2,\ L_3,\ L_4$), while the update law for the estimated vector $\widehat{\boldsymbol{\Theta}}$ will be subsequently designed. Therefore, the measurable product $Y\widehat{\boldsymbol{\Theta}}$ can be altered by modulating the length of the DMD surfaces. This term is designated as the auxiliary control input $\bar{\boldsymbol{u}} \in \mathbb{R}^3$

$$Y\widehat{\boldsymbol{\Theta}} \triangleq \bar{\boldsymbol{u}}. \tag{56}$$

To facilitate the subsequent stability analysis, let the desired auxiliary control signal $\bar{\boldsymbol{u}}_{\boldsymbol{d}} \in \mathbb{R}^3$ be designed as

$$\bar{\boldsymbol{u}}_{\boldsymbol{d}} \triangleq -K_1\boldsymbol{r} - \beta_1\boldsymbol{e_v}, \tag{57}$$

where $\beta_1 \in \mathbb{R}_{>0}$ is a positive constant gain, and $K_1 \in \mathbb{R}^{3\times 3}$ is a constant, positive-definite control gain matrix. Adding and subtracting $\bar{\boldsymbol{u}}_{\boldsymbol{d}}$ and substituting (56) and (57) into (55) yields the closed-loop error system

$$J\dot{\boldsymbol{r}} = Y\widetilde{\boldsymbol{\Theta}} + \widetilde{\boldsymbol{N}} + \boldsymbol{N_B} + \boldsymbol{\chi} - K_1\boldsymbol{r} - \beta_1\boldsymbol{e_v}, \tag{58}$$

where $\boldsymbol{\chi} \triangleq \bar{\boldsymbol{u}} - \bar{\boldsymbol{u}}_{\boldsymbol{d}} \in \mathbb{R}^3$ represents the mismatch between the desired and the actual auxiliary control inputs. Based on (58), the gradient-based adaptation law is designed as

$$\dot{\widehat{\boldsymbol{\Theta}}} \triangleq \operatorname{proj}(\Gamma Y^T\boldsymbol{r}), \tag{59}$$

where $\Gamma \in \mathbb{R}^{65\times 65}$ is a constant, positive-definite adaptation gain matrix, and $\mathrm{proj}(\cdot)$ denotes the continuous projection algorithm presented in [33]. Based on the value of $(\cdot)$ and the known bounds of $\widehat{\boldsymbol{\Theta}}$, the design in $\dot{\widehat{\boldsymbol{\Theta}}}$ ensures $\widehat{\boldsymbol{\Theta}}$ remains within the known bounded region without altering the stability of the system nor introducing undesired discontinuities.

5. Stability Analysis

To facilitate the stability analysis, some definitions are introduced. Let $\lambda_1,\ \lambda_2,\ \lambda_3,\ \lambda_4 \in \mathbb{R}_{>0}$ be defined as $\lambda_1 \triangleq \lambda_{\min}\{K_1\} - \zeta_5 - 1,\ \lambda_2 \triangleq \beta_1\lambda_{\min}\{\beta\}$, $\lambda_3 \triangleq \min(\lambda_1, \lambda_2)$, and $\lambda_4 \triangleq \lambda_3 - \frac{\sigma^2(\|\boldsymbol{\eta}\|)}{2}$, respectively, where β is the control gain defined in (32), $K_1,\ \beta_1$ are the control gains used in (57), $\sigma(\|\boldsymbol{\eta}\|)$ is the function defined in (38), $\zeta_5 \in \mathbb{R}_{>0}$ is a known bounding constant, and $\lambda_{\min}\{\cdot\} \in \mathbb{R}$ is the minimum eigenvalue of $\{\cdot\}$. Let the set $\mathcal{D}$ be defined as $\mathcal{D} \triangleq \left\{\boldsymbol{\eta} \,\middle|\, \|\boldsymbol{\eta}\| < \sigma^{-1}\left(\sqrt{2\lambda_3}\right)\right\}$, and let $\mathcal{S} \subset \mathcal{D}$ be defined as

$$\mathcal{S} \triangleq \left\{\boldsymbol{\eta} \in \mathcal{D} \,\middle|\, \|\boldsymbol{\eta}\| < \Lambda\right\}, \tag{60}$$

where $\Lambda \triangleq \sqrt{\frac{\underline{\lambda}}{\bar{\lambda}}\left(\sigma^{-1}\left(\sqrt{2\lambda_3}\right)\right)^2 - \frac{\bar{\zeta}-\underline{\zeta}}{\bar{\lambda}}}$, and $\underline{\lambda},\ \bar{\lambda},\ \underline{\zeta},\ \bar{\zeta} \in \mathbb{R}_{>0}$ are known bounding constants.

Theorem. Consider the spacecraft attitude dynamics governed by the nonlinear system in (1) with Assumptions 1-5. The auxiliary controller in (57) and the adaptive update law in (59) ensure uniformly ultimately bounded attitude tracking in the sense that

$$\|\boldsymbol{e_v}\| \leq \epsilon_1 \exp\{-\epsilon_2 t\} + \epsilon_3, \tag{61}$$

where $\epsilon_1 \triangleq \sqrt{\frac{\bar{\lambda}\|\boldsymbol{\eta}(0)\|^2 + \bar{\zeta}}{\underline{\lambda}}} \in \mathbb{R}_{>0}$, $\epsilon_2 \triangleq \frac{\lambda_4}{2\bar{\lambda}} \in \mathbb{R}_{>0}$, $\epsilon_3 \triangleq \sqrt{\frac{\bar{\lambda}}{\lambda_4\underline{\lambda}}\zeta_8 + \frac{\bar{\zeta}-\underline{\zeta}}{\underline{\lambda}}} \in \mathbb{R}_{>0}$, $\zeta_8 \triangleq \zeta_6 + \frac{(\zeta_4+\zeta_7)^2}{2} \in \mathbb{R}_{>0}$, and $\zeta_6,\ \zeta_7 \in \mathbb{R}_{>0}$ are known bounding constants. Provided that $\boldsymbol{\eta}(0) \in \mathcal{S}$ is satisfied, and that the control gains are selected sufficiently large such that $\lambda_1 > 0$, and $\Lambda > \epsilon_3$.

Proof. Let $V \in \mathbb{R}_{\geq 0}$ be a candidate Lyapunov function defined as

$$V(t) \triangleq \frac{1}{2}\boldsymbol{r}^T J \boldsymbol{r} + \beta_1 \boldsymbol{e_v}^{\boldsymbol{T}} \boldsymbol{e_v} + \beta_1(1-e_0)^2 + \frac{1}{2}\widetilde{\boldsymbol{\Theta}}^T \Gamma^{-1} \widetilde{\boldsymbol{\Theta}}. \tag{62}$$

The Lypaunov function can be upper and lower bounded as

$$\underline{\lambda}\|\boldsymbol{\eta}\|^2+\underline{\zeta} \leq V(t) \leq \bar{\lambda}\|\boldsymbol{\eta}\|^2+\bar{\zeta}. \tag{63}$$

Substituting (15), (16), (32), (54) and (58) into the time derivative of (62), and using the fact that $\boldsymbol{e_v}^T e_v{}^{\times}\tilde{\boldsymbol{\omega}} = 0$, yields

$$\begin{aligned} \dot{V}(t) = \boldsymbol{r}^T \left(Y\widetilde{\boldsymbol{\Theta}} + \widetilde{\boldsymbol{N}} + \boldsymbol{N_B} + \boldsymbol{\chi} - K_1\boldsymbol{r} \right) + \frac{1}{2}\boldsymbol{r}^T \dot{J}\boldsymbol{r} \\ - \beta_1 \boldsymbol{e_v}^T \beta \boldsymbol{e_v} + \widetilde{\boldsymbol{\Theta}}^T \Gamma^{-1}\dot{\boldsymbol{\Theta}} - \widetilde{\boldsymbol{\Theta}}^T \Gamma^{-1}\dot{\hat{\boldsymbol{\Theta}}}. \end{aligned} \tag{64}$$

Substituting the adaptive update law in (59) into (64), yields

$$\dot{V}(t) = \boldsymbol{r}^T \widetilde{\boldsymbol{N}} + \boldsymbol{r}^T \boldsymbol{N_B} + \boldsymbol{r^T}\boldsymbol{\chi} - \boldsymbol{r}^T K_1 \boldsymbol{r} - \beta_1 \boldsymbol{e_v}^T \beta \boldsymbol{e_v} + \frac{1}{2}\boldsymbol{r}^T \dot{J}\boldsymbol{r} + \widetilde{\boldsymbol{\Theta}}^T \Gamma^{-1}\dot{\boldsymbol{\Theta}}. \tag{65}$$

In (64), the last two terms can be upper bounded using Assumptions 3 and 6 as

$$\frac{1}{2}\boldsymbol{r}^T \dot{J}\boldsymbol{r} \leq \zeta_5 \|\boldsymbol{r}\|^2, \tag{66}$$

$$\widetilde{\boldsymbol{\Theta}}^T \Gamma^{-1}\dot{\boldsymbol{\Theta}} \leq \zeta_6. \tag{67}$$

Using (38), (39), (66) and (67), (65) can be upper bounded as

$$\begin{aligned} \dot{V}(t) \leq & - \left(\lambda_{\min}\{K_1\} - \zeta_5\right) \|\boldsymbol{r}\|^2 \\ & - \beta_1 \lambda_{\min}\{\beta\} \|\boldsymbol{e_v}\|^2 + \sigma(\|\boldsymbol{\eta}\|)\|\boldsymbol{\eta}\|\|\boldsymbol{r}\| + \left(\zeta_4 + \|\boldsymbol{\chi}\|\right)\|\boldsymbol{r}\| + \zeta_6. \end{aligned} \tag{68}$$

Assumption 7. A numerical optimization algorithm can be used to find a suitable set of DMD surface lengths (i.e., L_1, L_2, L_3 and L_4) that minimizes $\|\boldsymbol{\chi}\|$, and the resulting $\boldsymbol{\chi}$ can be upper bounded by a constant for the entire maneuver such that $\|\boldsymbol{\chi}\| \leq \zeta_7$. $\square$

Using Young's inequality on the term $\sigma(\|\boldsymbol{\eta}\|)\|\boldsymbol{\eta}\|\|\boldsymbol{r}\|$ yields $\sigma(\|\boldsymbol{\eta}\|)\|\boldsymbol{\eta}\|\|\boldsymbol{r}\| \leq \frac{\sigma^2(\|\boldsymbol{\eta}\|)\|\boldsymbol{\eta}\|^2}{2} + \frac{1}{2}\|\boldsymbol{r}\|^2$. Similarly, the inequality $\left(\zeta_4 + \|\boldsymbol{\chi}\|\right)\|\boldsymbol{r}\| \leq \frac{1}{2}\|\boldsymbol{r}\|^2 + \frac{(\zeta_4+\zeta_7)^2}{2}$ can be obtained using Assumption 7. Therefore, (68) can be rewritten as

$$\dot{V}(t) \leq -\lambda_1 \|\boldsymbol{r}\|^2 - \lambda_2 \|\boldsymbol{e_v}\|^2 + \frac{\sigma^2(\|\boldsymbol{\eta}\|)\|\boldsymbol{\eta}\|^2}{2} + \zeta_8. \tag{69}$$

The expression in (69) can be further upper bounded as

$$\dot{V}(t) \leq -\left(\lambda_3 - \frac{\sigma^2(\|\boldsymbol{\eta}\|)}{2}\right)\|\boldsymbol{\eta}\|^2 + \zeta_8. \tag{70}$$

Provided $\boldsymbol{\eta} \in \mathcal{D}$, then (70) can be rewritten as

$$\dot{V}(t) \leq -\lambda_4\|\boldsymbol{\eta}\|^2 + \zeta_8 \quad \forall \boldsymbol{\eta} \in \mathcal{D}. \tag{71}$$

Using the bounds in (63), (71) can be rewritten as

$$\dot{V}(t) \leq -\frac{\lambda_4}{\overline{\lambda}}V(t) + \epsilon_0, \tag{72}$$

where $\epsilon_0 \triangleq \zeta_8 + \frac{\lambda_4 \overline{\zeta}}{\overline{\lambda}}$. By invoking the Comparison Lemma from [34], the solution to (72) can be obtained as

$$V(t) \leq \exp\left\{-\frac{\lambda_4}{\overline{\lambda}}t\right\}V(0) + \frac{\overline{\lambda}}{\lambda_4}\epsilon_0\left(1 - \exp\left\{-\frac{\lambda_4}{\overline{\lambda}}t\right\}\right). \tag{73}$$

Using (63) and (73) yields

$$\|\boldsymbol{\eta}\|^2 \leq \left(\frac{\overline{\lambda}\|\boldsymbol{\eta}(0)\|^2 + \overline{\zeta}}{\underline{\lambda}}\right)\exp\left\{-\frac{\lambda_4}{\overline{\lambda}}t\right\} + \left(\frac{\overline{\lambda}}{\lambda_4\underline{\lambda}}\zeta_8 + \frac{\overline{\zeta} - \underline{\zeta}}{\underline{\lambda}}\right). \tag{74}$$

Using (40) and (74) yields the uniformly ultimately bounded result in (61) provided $\boldsymbol{\eta}(0) \in \mathcal{S}$, where uniformity in initial time can be concluded from the independence of λ_3 and the ultimate bound from ϵ_3 at time $t = 0$. From (62), (63) and (73), then $\boldsymbol{r} \in \mathcal{L}_\infty$. Then, from (17) and (32), $\boldsymbol{\omega} \in \mathcal{L}_\infty$. Similarly, from (15) and (16), $\dot{\boldsymbol{e}}_{\boldsymbol{v}}, \dot{e}_0 \in \mathcal{L}_\infty$. Since $\boldsymbol{r}, \boldsymbol{\omega} \in \mathcal{L}_\infty$, and $\boldsymbol{e}_v, e_0, \boldsymbol{\omega}_{\boldsymbol{d}} \in \mathcal{L}_\infty$ by definition, then $\bar{\boldsymbol{u}}_{\boldsymbol{d}} \in \mathcal{L}_\infty$ by (57). Since $\widehat{\boldsymbol{\Theta}} \in \mathcal{L}_\infty$ by (59), $\bar{\boldsymbol{u}}_{\boldsymbol{d}} \in \mathcal{L}_\infty$, and $\boldsymbol{\chi} \in \mathcal{L}_\infty$ by Assumption 7, therefore $Y \in \mathcal{L}_\infty$ using (56). ■

6. Simulation Results

The simulations presented in this section are performed using the 4th order Runge-Kutta fixed-step algorithm to propagate the orbital and attitude dynamics. The first simulation, in Subsection 6.1, illustrates the performance of the controller when required to achieve a fixed orientation relative to the orbital frame (regulation maneuver). The second simulation, in Subsection 6.2, presents the result obtained using the controller to track a time-varying reference relative to the orbital frame (tracking maneuver). Effects of aerodynamic drag and lift, gravity gradient torque and J_2 perturbation are included in the spacecraft dynamics. The NRLMSISE-00 atmospheric model is used as the true (unknown for the controller) atmospheric density. The control law in (57) is computed every 30 seconds to allow finding a suitable set of DMD surfaces lengths through the formulation of a constrained function minimization problem that minimizes $\|\boldsymbol{\chi}\|$, and includes the physical length constraints of the DMD surfaces. The MATLAB *fmincon* command is used to solve the minimization problem

$$\min_{L_1, L_2, L_3, L_4} \|Y\widehat{\boldsymbol{\Theta}} - \bar{\boldsymbol{u}}_{\boldsymbol{d}}\| \quad \text{subject to} \quad \left\{ 0 \leq L_j \leq 3.7, \quad j = 1, 2, 3, 4. \right. \tag{75}$$

The spacecraft is simulated in a circular orbit with inclination of 51.94 degrees and 400 km altitude, similar to that of the International Space Station (ISS). The initial orbital elements and spacecraft parameters are presented in Tables 1 and 2, respectively. Additionally, the simulations also incorporate modeling inaccuracies in the CoM location and inertia matrix. For visualization purposes, in the subsequent simulation results, the orientation of the body with respect to the orbital frame is expressed using a 3-2-1 Euler angle sequence, where ϕ, θ and ψ denote the roll, pitch and yaw angles, respectively (see [17] for details). The roll, pitch and yaw angles correspond to rotations about $\hat{\boldsymbol{b}}_{\boldsymbol{1}}$, $\hat{\boldsymbol{b}}_{\boldsymbol{2}}$ and $\hat{\boldsymbol{b}}_{\boldsymbol{3}}$, respectively. Simulation parameters, initial conditions and uncertainties are the same for both simulation examples. The initial conditions (ϕ_0, θ_0, ψ_0) are presented in Table 3.

Parameter	Value
Semi-Major Axis $[m]$	6778×10^3
Eccentricity	0
Inclination $[deg]$	51.94
RAAN $[deg]$	206.26
Arg. of Perigee $[deg]$	101.07
True Anomaly $[deg]$	108.08

Table 1: Initial orbital parameters for simulation of regulation and tracking maneuvers.

Parameter	Value
CubeSat Body Mass $[kg]$	3
DMD Surface Mass $[kg]$	9×10^{-2}
Max. DMD Surface Length $[m]$	3.7
DMD Surface Width $[m]$	3.8×10^{-2}

Table 2: Spacecraft parameters for simulation of regulation and tracking maneuvers.

Parameter	Value
ϕ_0 $[deg]$	45
θ_0 $[deg]$	-60
ψ_0 $[deg]$	50
$\dot{\phi}_0$ $[deg/s]$	5×10^{-2}
$\dot{\theta}_0$ $[deg/s]$	-7.5×10^{-2}
$\dot{\psi}_0$ $[deg/s]$	6×10^{-2}

Table 3: Initial Euler angles and angle rates for simulation of regulation and tracking maneuvers.

6.1. Regulation Maneuver

To propagate the spacecraft dynamics, a model to compute the inertia matrix J_m as function of the DMD-surfaces lengths is used. Specifically, J_m is computed by representing a 2U CubeSat structure as a rectangular box, and the rolled and deployed portions of a DMD-surface are modeled as a thick walled cylinder and a flat plate, respectively. The inaccuracy of J_m is introduced by incorporating deviations in the mass for each part of the spacecraft and the assumed locations of their individual CoMs are shown in Table 4.

Parameter	Real (for J)	Approx. (for J_m)
CoM CubeSat Body [cm]	$[0\ 0\ 0]^T$	$[1.8\ 2\ -3]^T$
CoM Flat Plate $(\times 10^{-2})$ [m]	$[0\ 0\ 0]^T$	$[4.5L_j^2\ 0\ 0]^T$
Deployer mass [g]	89.88	75

Table 4: Uncertainties included in simulation to compute J_m. CoMs expressed in coordinate systems centered at the geometric center of the body of interest, where $j = 1,\ 2,\ 3,\ 4$.

The objective for this maneuver is to achieve a fixed orientation of the spacecraft with respect to the orbital frame. The controller parameters are shown in Table 5, and the desired Euler angles are presented in Table 6. Figures 3 and 4 show the resulting quaternion error components and the corresponding transformation to Euler angles for a 10 hour simulation, respectively. The results show that the regulation objective was achieved with ultimate bounds for roll, pitch and yaw within ± 3, ± 2 and ± 2.2 degrees, respectively.

As concluded in the stability analysis, the resulting ultimate bound can be attributed to the size of the disturbance torques in $\boldsymbol{\delta}$, the residual error $\boldsymbol{\chi}$, the unmodeled effects of the DMD on the inertia matrix, and the rate of change of the uncertain parameters (i.e., $\dot{\boldsymbol{\Theta}}$). Therefore, efforts on improving the knowledge of the inertia matrix, using a good numerical algorithm to solve for the lengths and avoiding high deployment rates, would have direct influence on reducing the ultimate bounds.

The levels of deployment for the DMD surfaces are shown in Figure 5. Actuator saturation was applied to account for the physical limits of the DMD surfaces. Although this saturation was not explicitly modeled in the controller design, the controller has shown to be robust enough to regulate the orientation despite the physical actuator limits. In an effort to reduce the influence of rapid variations of the control inputs, a low-pass filter with cutoff frequency $\omega_c \triangleq 0.017$ Hz has been applied to the lengths calculated by the *fmincon* algorithm and the maximum deployment rate among all DMD surfaces for this maneuver was 2.9 meters per minute. The norm of the resulting mismatch between $\bar{\boldsymbol{u}}$ and $\bar{\boldsymbol{u}}_{\boldsymbol{d}}$ (i.e., $\|\boldsymbol{\chi}\|$) is shown in Figure 6. Due to the amplitude limitations of the environmental torques, the actuators reached their saturation limits multiple times during approximately the first five hours of the maneuver. However, after the period of saturation, $\|\boldsymbol{\chi}\|$ remained below 1×10^{-6} Nm.

The estimated parameters in $\widehat{\boldsymbol{\Theta}}$ are shown in Figures 7 and 8 for the parameters associated with the aerodynamic drag and in Figures 9 and 10 for the parameters associated with the aerodynamic lift. The estimations are divided into four plots to better observe their variation over time because of their different orders of magnitude. From the stability analysis, it cannot be concluded that the estimation error $\widetilde{\boldsymbol{\Theta}}$ converges to zero, meaning that there is no on-line parameter estimation. However, the results show that all parameters are dynamically adjusted to compensate for the environmental and physical uncertainties and remain bounded.

Parameter	Value
$K_1\ (\times 10^{-3})$	$\mathrm{diag}(3, 3, 3)$
$\beta\ \left(\times 10^{-3}\right)$	$\mathrm{diag}(1.5, 5, 5)$
$\beta_1\ \left(\times 10^{-6}\right)$	3.2
Γ	$\mathrm{diag}\left(\Gamma_2, \Gamma_2, \Gamma_2, \Gamma_2, 6\Gamma_2, 6\Gamma_2, \Gamma_1, \Gamma_1, 10^{-20}\right)$
$\Gamma_1\ \left(\times 10^{-19}\right)$	$\mathrm{diag}\left(1, 10^{11}, 1, 10^{11}, 1, 10^{11}, 1, 10^{11}\right)$
$\Gamma_2\ \left(\times 10^{-22}\right)$	$\mathrm{diag}\left(2, 2^{11}, 2, 2^{11}, 2, 2^{11}, 2, 2^{11}\right)$

Table 5: Controller parameters used for simulation of regulation and tracking maneuvers.

ϕ_d $[deg]$	θ_d $[deg]$	ψ_d $[deg]$
45	0	10

Table 6: Desired orientation of the spacecraft with respect to the orbital frame for the regulation maneuver.

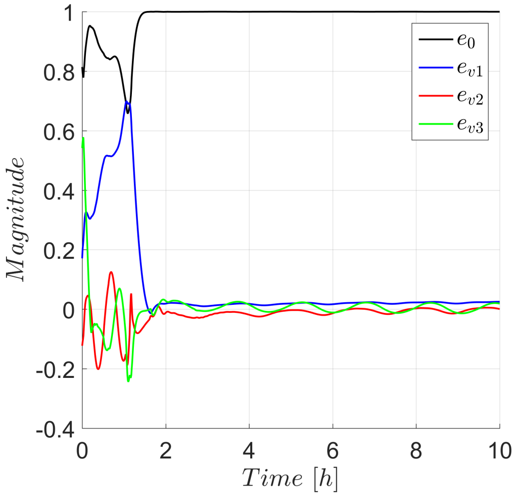

Figure 3: Resulting error quaternion for the regulation maneuver using the designed controller.

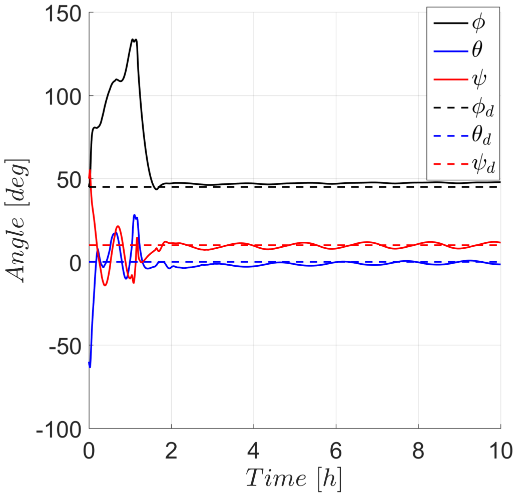

Figure 4: Resulting Euler angles for the regulation maneuver using the designed controller.

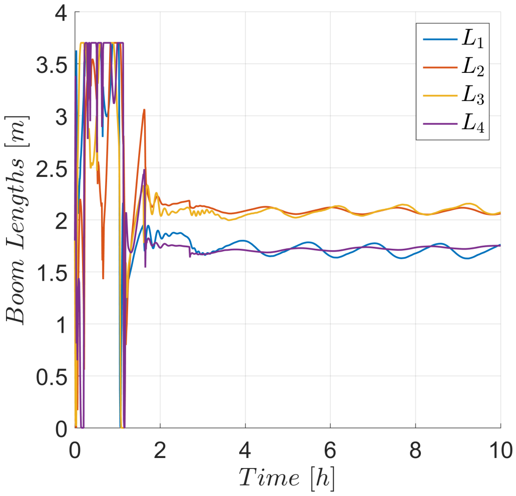

Figure 5: Required level of deployment for the DMD surfaces using the designed controller for the regulation maneuver.

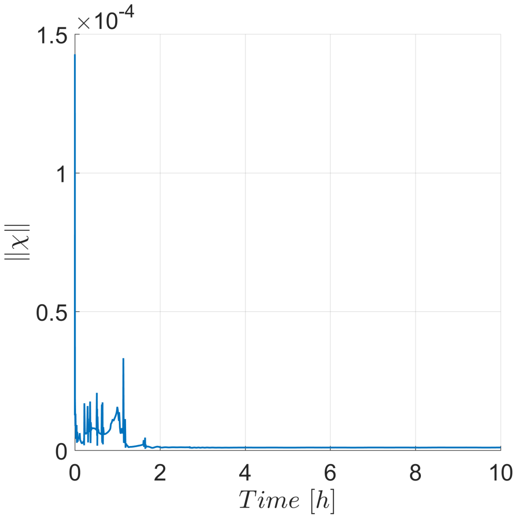

Figure 6: Resulting mismatch $\|\boldsymbol{\chi}\|$ obtained using MATLAB *fmincon* to solve for the DMD surfaces lengths for the regulation maneuver.

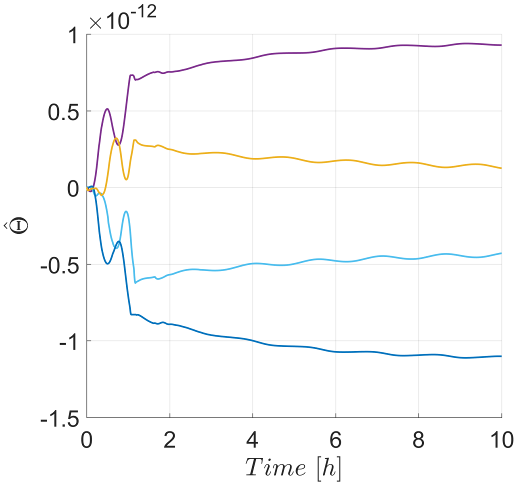

Figure 7: Resulting parameter estimates $\widehat{B}_1\widehat{C}_{D,j}$ in $\widehat{\boldsymbol{\Theta}}$ with $j = 1, 2, 3, 4$ associated with the aerodynamic drag for the regulation maneuver using the designed controller.

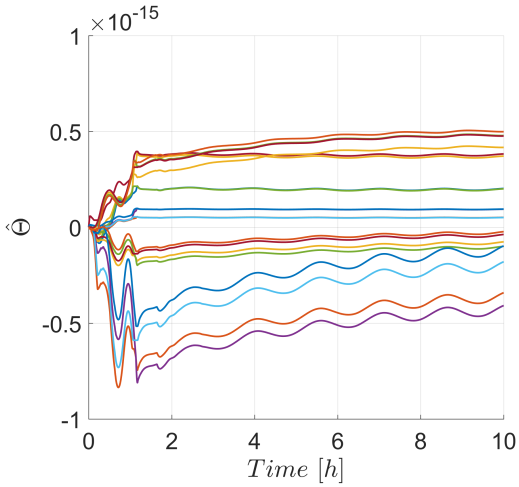

Figure 8: Resulting parameter estimates $\left[\hat{c}_1\widehat{B}_1\widehat{C}_{D,j},\ \hat{c}_1\widehat{B}_2\widehat{C}_{D,j},\ \hat{c}_2\widehat{B}_1\widehat{C}_{D,j},\ \hat{c}_2\widehat{B}_2\widehat{C}_{D,j},\ \hat{c}_3\widehat{B}_1\widehat{C}_{D,j},\ \hat{c}_3\widehat{B}_2\widehat{C}_{D,j}\right]^T$ in $\widehat{\mathbf{\Theta}}$ with $j = 1,2,3,4$ associated with the aerodynamic drag for the regulation maneuver using the designed controller.

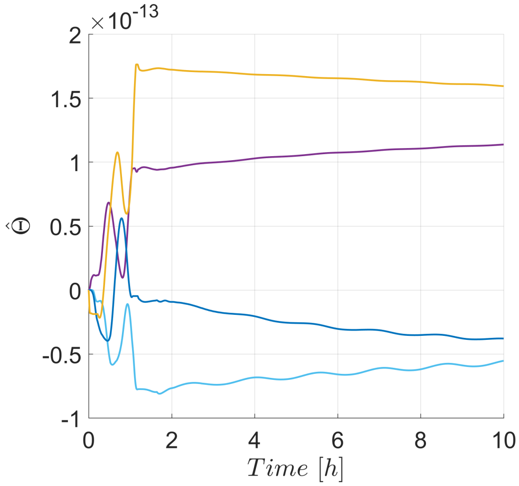

Figure 9: Resulting parameter estimates $\widehat{B}_1\widehat{C}_{L,j}$ in $\widehat{\mathbf{\Theta}}$ with $j = 1,2,3,4$ associated with the aerodynamic lift for the regulation maneuver using the designed controller.

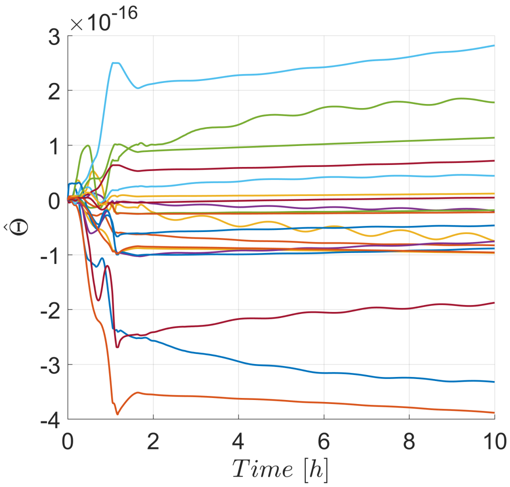

Figure 10: Resulting parameter estimates $\left[\hat{c}_1\widehat{B}_1\widehat{C}_{L,j},\ \hat{c}_1\widehat{B}_2\widehat{C}_{L,j},\ \hat{c}_2\widehat{B}_1\widehat{C}_{L,j},\ \hat{c}_2\widehat{B}_2\widehat{C}_{L,j},\ \hat{c}_3\widehat{B}_1\widehat{C}_{L,j},\ \hat{c}_3\widehat{B}_2\widehat{C}_{L,j}\right]^T$ in $\widehat{\boldsymbol{\Theta}}$ with $j = 1, 2, 3, 4$ associated with the aerodynamic lift for the regulation maneuver using the designed controller.

For the specific spacecraft and orbit considered in the regulation example, a feasible range of operation including saturation of the control inputs is determined by performing a set of 1000 five-hour simulations of regulation maneuvers. The initial conditions and the desired Euler angles are randomly initialized as shown in Table 7. The set of possible desired Euler angles has been selected so that the operational range for a more demanding mission as compared to the previous example is considered (e.g., pointing a camera on the ram/anti-ram face of the spacecraft to a given objective).

To point the $\hat{\boldsymbol{b}}_{\mathbf{1}}$ body axis towards any direction inside a cone of limited size with respect to the along-track direction $\hat{\boldsymbol{o}}_{\mathbf{1}}$, it is sufficient to vary the desired roll and yaw angles. The size of the cone is driven by the bounds of the yaw angle and all directions inside the cone are explored by varying the roll angle. For all simulations, the spacecraft is considered stabilized if $\|\boldsymbol{e_v}\| \leq 0.4$ (user-defined) on average during the last 20 minutes of the maneuver, which was found representative for successful maneuvers considering the ultimately bounded result from the stability analysis. Figure 11 presents the percentage of stabilized maneuvers with different limits for the norm of the yaw angle $\|\psi\|$ (i.e., cone sizes). Figure 12 illustrates the difference in size between cones resulting from yaw bounds of ±8 and ±25 degrees, with percentages of success of 80% and 70%, respectively. The remaining percentage of failure can be attributed to several factors including the limitations due to the DMD geometry, initial conditions, and variations of atmospheric density, among others.

Parameter	Range
$\phi_0,\ \theta_0,\ \psi_0$ [deg]	$[-10, 10]$
$\dot{\phi}_0,\ \dot{\theta}_0,\ \dot{\psi}_0$ [deg/s]	$[-0.02, 0.02]$
ϕ_d [deg]	$[-180, 180]$
θ_d [deg]	0
ψ_d [deg]	$[-25, 25]$

Table 7: Parameter ranges for the set of 1000 five-hour simulations.

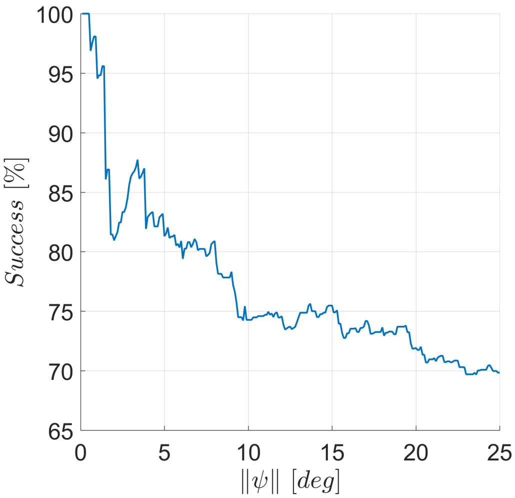

Figure 11: Resulting percentage of successful regulation maneuvers vs. size of the cone.

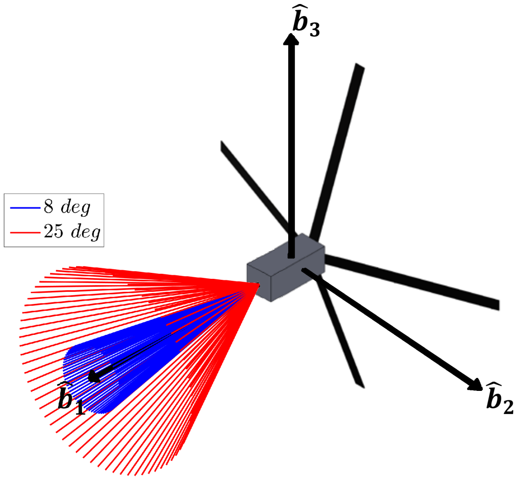

Figure 12: Resulting feasible range of operation, 8 degrees (80%), 25 degrees (70%).

6.2. Tracking Maneuver

The simulation presented in this subsection illustrates a scenario where the CubeSat is required to change its orientation with respect to the orbital frame over time. This task could be required for missions where the spacecraft needs to adjust its orientation for pointing a sensor (e.g., a camera) towards different areas during the mission. The scenario considers a spacecraft that is required to track a desired trajectory of the roll angle while keeping the pitch and yaw angles fixed. The initial conditions and control parameters are the same used for the regulation maneuver, and the desired Euler angles are presented in Table 8.

Figures 13 and 14 show the resulting quaternion error components and the corresponding transformation to Euler angles for a 10 hour simulation. These results show that the CubeSat orientation reaches the ultimate bound in approximately 5 hours. The ultimate bounds for roll, pitch and yaw are ± 3, ± 1.5 and ± 3 degrees, respectively.

The resulting lengths of the DMD are shown in Figure 15, where saturation to account for the physical constraints was applied. The DMD surfaces reached their saturation levels multiple times during the first two hours of the simulation, and the controller has shown to be robust during that portion of the maneuver. The maximum deployment rate among all DMD surfaces for the tracking maneuver was 2.6 meters per minute. Figure 16 shows the norm of the mismatch between $\bar{\boldsymbol{u}}$ and $\bar{\boldsymbol{u}}_{\boldsymbol{d}}$ (i.e., $\|\boldsymbol{\chi}\|$), after the period of saturation, it remained below 8.9×10^{-7} Nm.

The estimated parameters in $\widehat{\boldsymbol{\Theta}}$ are shown in Figures 17 and 18 for parameters associated with the aerodynamic drag and in Figures 19 and 20 for those associated with the aerodynamic lift. All the estimations remain bounded and are dynamically adjusted to compensate for the uncertainties but on-line estimation cannot be guaranteed.

ϕ_d $[deg]$	θ_d $[deg]$	ψ_d $[deg]$
$35 + 15\sin(4.36 \times 10^{-4}t)$	0	0

Table 8: Desired orientation of the spacecraft with respect to the orbital frame for the tracking maneuver.

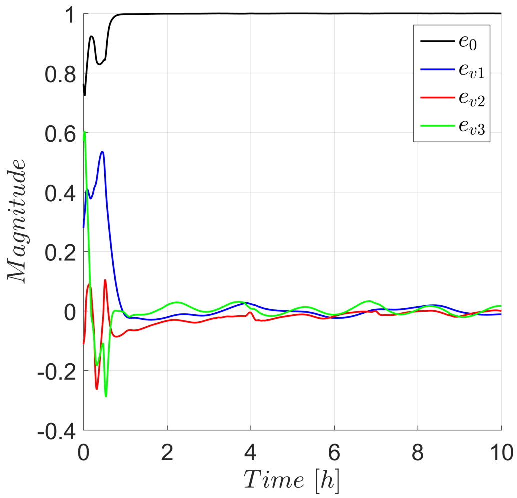

Figure 13: Resulting error quaternion for the tracking maneuver using the designed controller.

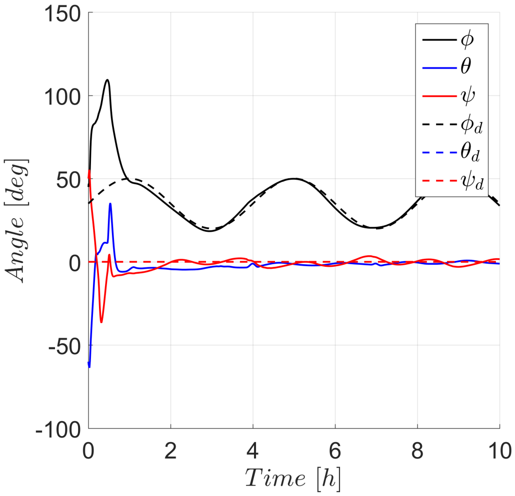

Figure 14: Resulting Euler angles for the tracking maneuver using the designed controller.

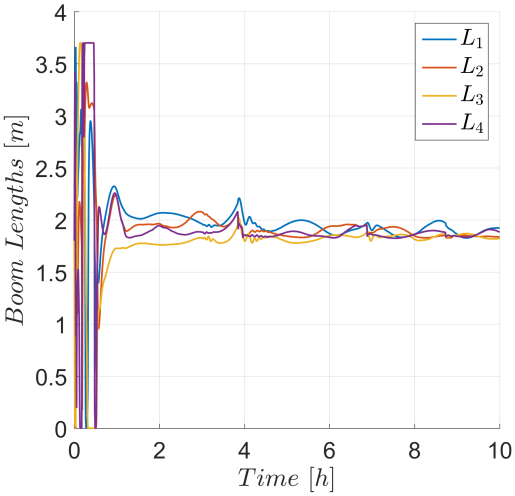

Figure 15: Required level of deployment for the DMD surfaces using the designed controller for the tracking maneuver.

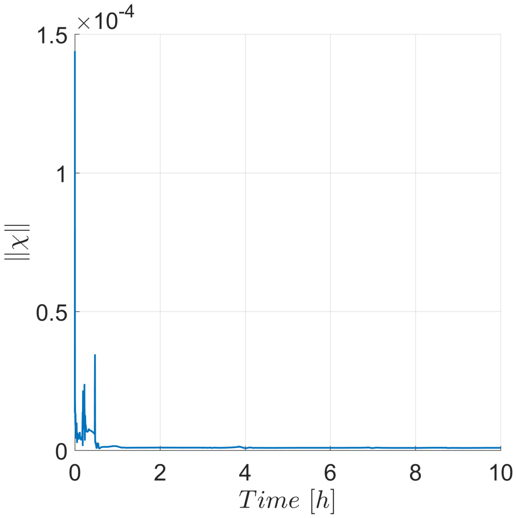

Figure 16: Resulting mismatch $\|\boldsymbol{\chi}\|$ obtained using MATLAB *fmincon* to solve for the DMD surfaces lengths for the tracking maneuver.

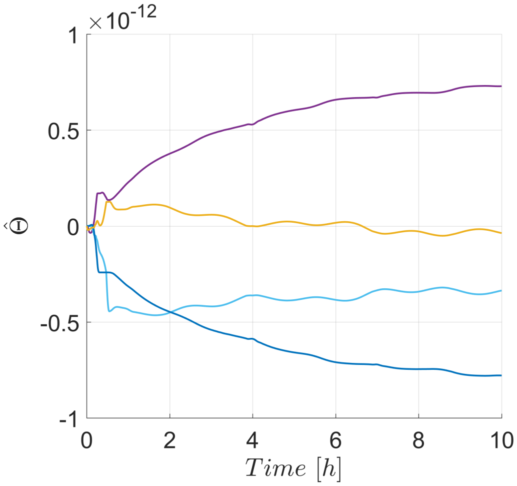

Figure 17: Resulting parameter estimates $\widehat{B}_1\widehat{C}_{D,j}$ in $\widehat{\boldsymbol{\Theta}}$ with $j = 1, 2, 3, 4$ associated with the aerodynamic drag for the tracking maneuver using the designed controller.

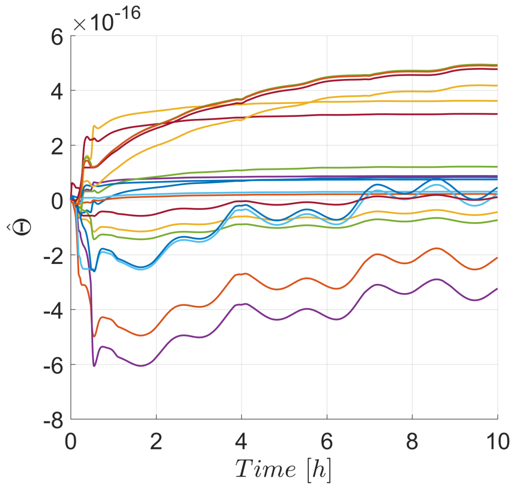

Figure 18: Resulting parameter estimates $\left[\hat{c}_1\widehat{B}_1\widehat{C}_{D,j},\ \hat{c}_1\widehat{B}_2\widehat{C}_{D,j},\ \hat{c}_2\widehat{B}_1\widehat{C}_{D,j},\ \hat{c}_2\widehat{B}_2\widehat{C}_{D,j},\ \hat{c}_3\widehat{B}_1\widehat{C}_{D,j},\ \hat{c}_3\widehat{B}_2\widehat{C}_{D,j}\right]^T$ in $\widehat{\boldsymbol{\Theta}}$ with $j = 1, 2, 3, 4$ associated with the aerodynamic drag for the tracking maneuver using the designed controller.

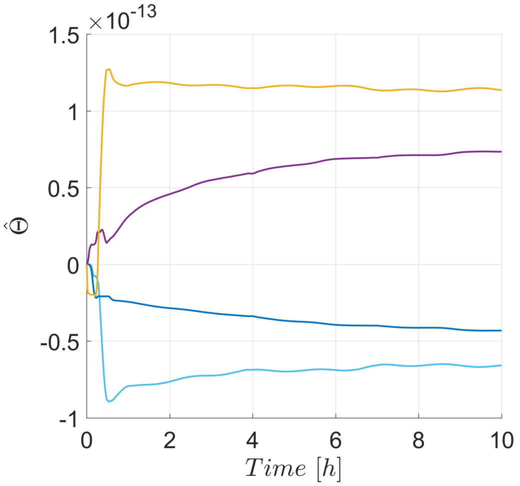

Figure 19: Resulting parameter estimates $\widehat{B}_1\widehat{C}_{L,j}$ in $\widehat{\boldsymbol{\Theta}}$ with $j = 1, 2, 3, 4$ associated with the aerodynamic lift for the tracking maneuver using the designed controller.

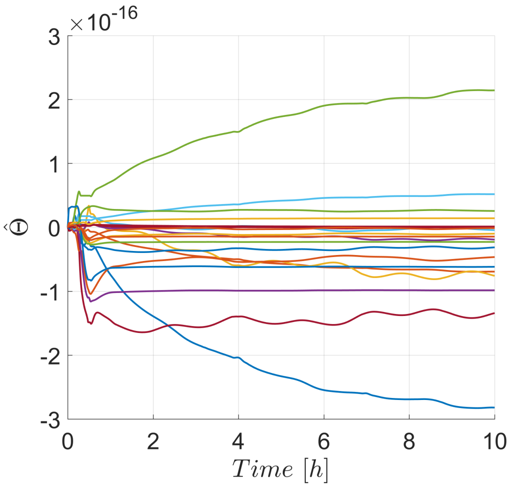

Figure 20: Resulting parameter estimates $\left[\hat{c}_1\widehat{B}_1\widehat{C}_{L,j},\ \hat{c}_1\widehat{B}_2\widehat{C}_{L,j},\ \hat{c}_2\widehat{B}_1\widehat{C}_{L,j},\ \hat{c}_2\widehat{B}_2\widehat{C}_{L,j},\ \hat{c}_3\widehat{B}_1\widehat{C}_{L,j},\ \hat{c}_3\widehat{B}_2\widehat{C}_{L,j}\right]^T$ in $\widehat{\boldsymbol{\Theta}}$ with $j = 1, 2, 3, 4$ associated with the aerodynamic lift for the tracking maneuver using the designed controller.

To illustrate the approach taken to evaluate the effect that the applied torques may have on the long DMD surfaces, a comparison between the frequency content of the applied torque and the first natural frequencies of a DMD surface was performed for the tracking maneuver. A fully deployed DMD surface was modeled as a cantilevered beam and the first natural frequencies were computed using SolidWorks. Figure 21 illustrates the first five mode shapes and their corresponding frequencies, and Figure 22 shows the Fast Fourier Transform (FFT) of each component of the applied torque. From these figures, the range of frequencies of the applied torques is reasonably below the first natural frequency of the DMD surface (i.e., 0.1396 Hz).

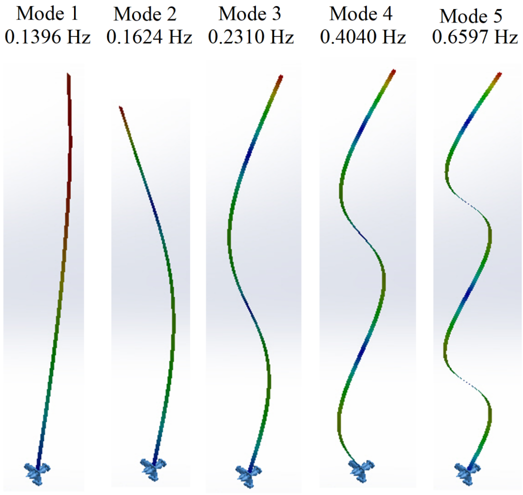

Figure 21: First natural frequencies of a fully deployed DMD surface.

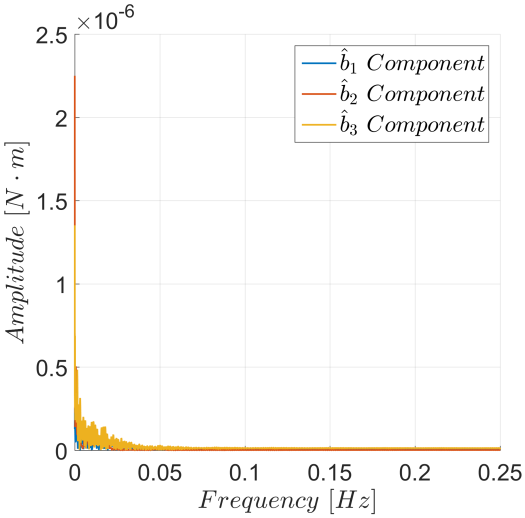

Figure 22: FFT of the torque $Y\widehat{\boldsymbol{\Theta}}$ applied during the tracking maneuver.

7. Conclusion

This paper presented the design and validation through numerical simulation of an adaptive controller for environmental torques-based attitude control that compensates for uncertainties in the atmospheric density, drag and lift coefficients, and center of mass location. Moreover, the controller also considers perturbations associated with the non-modeled behavior of the inertia matrix. The obtained result ensures the alignment of the body and orbital frames within ultimate bounds. Simulation results including aerodynamic and gravity gradient torques, actuator saturation, as well as the NRLMSISE-00 model for atmospheric density and J_2 perturbation, were performed to validate regulation and tracking of the angles to their desired values relative to the orbital frame within bounds of ± 3 deg. Therefore, the controller shows potential for applications where the location of the center of mass, atmospheric density, drag coefficients are uncertain and the inertia matrix cannot be accurately computed in real time. Future work on this problem will consider strategies to address implementation challenges such as failures to deploy a DMD surface.

Acknowledgments

This research has been supported by the Fulbright Colombia Commission and the AFOSR award number FA9550-19-1-0169. Any opinions, findings and conclusions or recommendations expressed in this material are those of the authors and do not necessarily reflect the views of the sponsoring agency.

References

[1] T. C. Program, Cubesat design specification rev.13 (2015).

[2] M. I. Martinelli, R. S. Sanchez-Peña, Passive 3 axis attitude control of msu-1 pico-satellite, Acta Astronautica 56 (2005) 507–517. `doi:10.1016/j.actaastro.2004.10.007`.

[3] M. Pastorelli, R. Bevilacqua, S. Partorelli, Differential-drag-based roto-translational control for propellant-less spacecraft, Acta Astronautica 114 (2015) 6–21. `doi:j.actaastro.2015.04.014`.

[4] R. Sun, J. Wang, D. Zhang, Q. Jia, X. Shao, Roto-translational spacecraft formation control using aerodynamic forces, Journal of Guidance, Control and Dynamics 40 (10) (2017) 2556–2568. `doi:10.2514/1.G003130`.

[5] R. Sutherland, I. Kolmanovsky, A. R. Girard, Attitude control of a 2u cubesat by magnetic and air drag torques, IEEE Transactions on Control Systems Technology 27 (3) (2019) 1047–1059. `doi:10.1109/TCST.2018.2791979`.

[6] A. Harris, C. D. Petersen, H. Schaub, Linear coupled attitude-orbit control through aerodynamic forces, AIAA Journal of Guidance, Control and Dynamics 43 (1) (2020) 122–131. `doi:10.2514/1.G004521`.

[7] C. L. Leonard, M. Hollister, E. V. Bergman, Orbital formationkeeping with differential drag, Journal of Guidance, Control and Dynamics 12 (1) (1989) 108–113. `doi:10.2514/3.20374`.

[8] R. Bevilacqua, M. Romano, Rendezvous maneuvers of multiple spacecraft by differential drag under j2 perturbation, Journal of Guidance, Control and Dynamics 31 (6) (2008) 1595–1607. `doi:10.2514/1.36362`.

[9] M. Horsley, S. Nikolaev, A. Pertica, Rendezvous maneuvers of small spacecraft using differential lift and drag, Journal of Guidance, Control and Dynamics 36 (2) (2011) 445–453. `doi:10.2514/1.57327`.

[10] R. Perez, D. an Bevilacqua, Differential drag spacecraft rendezvous using an adaptive lyapunov control strategy, Acta Astronautica 83 (2013) 196–207. `doi:10.1016/j.actaastro.2012.09.005`.

[11] D. Ivanov, M. Kushniruk, M. Ovchinnikov, Study of satellite formation flying control usign differential lift and drag, Acta Astronautica 152 (2018) 88–100. `doi:10.1016/j.actaastro.2018.07.047`.

[12] D. Guglielmo, S. Omar, R. Bevilacqua, L. Fineberg, J. Treptow, B. Poffenberger, Y. Johnson, Drag de-orbit device: A new standard reentry actua-

tor for cubesats, Journal of Spacecraft and Rockets 56 (1) (2018) 129–145. `doi:10.2514/1.A34218`.

[13] S. Omar, D. Guglielmo, R. Bevilacqua, Drag de-orbit device (d3) mission for validation of controlled spacecraft re-entry using aerodynamic drag, in: 4th IAA Dynamics and Control of Space Systems Conference, Rome, Italy., 2017.

[14] S. Omar, R. Bevilacqua, Hardware and GNC solutions for controlled spacecraft re-entry using aerodynamic drag, Acta Astronautica 159 (2019) 49–64. `doi:j.actaastro.2019.03.051`.

[15] C. Riano-Rios, R. Bevilacqua, W. E. Dixon, Adaptive control for differential drag-based rendezvous maneuvers with an unknown target, Acta Astronautica, In Press. `doi:j.actaastro.2020.03.011`.

[16] C. Riano-Rios, R. Bevilacqua, W. E. Dixon, Differential drag-based multiple spacecraft maneuvering and on-line parameter estimation using integral concurrent learning, Acta Astronautica 174 (2020) 189–203. `doi:j.actaastro.2020.04.059`.

[17] C. Riano-Rios, S. Omar, R. Bevilacqua, W. E. Dixon, Spacecraft attitude regulation in low earth orbit using natural torques, in: 2019 IEEE 4th Colombian Conference on Automatic Control (CCAC), Medellin, Colombia., 2019.

[18] S. Omar, C. Riano-Rios, R. Bevilacqua, Semi-passive three axis attitude stabilization for earth observation satellites using the drag maneuvering device, in: 12th Symposium on Small Satellite for Earth Observation. Berlin, Germany, 2019.

[19] R. Sun, C. Riano-Rios, R. Bevilacqua, N. G. Fitz-Coy, W. E. Dixon, Cubesat adaptive attitude control with uncertain drag coefficient and atmospheric density, AIAA Journal of Guidance, Control and Dynamics, to appear.

[20] J. Virgili-Llop, H. C. Polat, M. Romano, Attitude stabilization of spacecraft in very low earth orbit by center-of-mass shifting, Frontiers in Robotics and AI 6 (2019) 1–9. `doi:https://doi.org/10.3389/frobt.2019.00007`.

[21] I. Palunko, R. Fierro, Adaptive control of a quadrotor with dynamic changes in the center of gravity, in: Proceedings of the 18th IFAC World Congress, Milano, Italy., 2011.

[22] D. Thakur, S. Srikant, M. R. Akella, Adaptive attitude-tracking control of spacecraft with uncertain time-varying inertia parameters, Journal of Guidance, Control, and Dynamics 38 (1) (2015) 41–52. `doi:10.2514/1.G000457`.

[23] J. R. Wertz, D. F. Everett, J. Puschell, Space mission engineering: the new SMAD, 3rd Edition, Microcosm Press, 2011.

[24] E. P. Blackburn, D. DeBra, D. Dobrotin, J. Scull, R. E. Fischell, D. Fosth, J. Kelly, A. J. Fleig, H. Perkel, R. E. Roberson, J. Rodden, B. Tinling, S. O'Neil, F. J. Carroll, R. F. Bohling, NASA space vehicle design criteria monograph (guidance and control), NASA SP-8018.

[25] P. Hughes, Spacecraft Attitude Dynamics, Dover Books on Aeronautical Engineering, Dover Publications, 2012.

[26] NOAA, U.S. standard atmosphere (1976).

[27] I. Harris, W. Priester, Time-dependent structure of the upper atmosphere, Journal of the Atmospheric Sciences 19 (4) (1962) 286–301. `doi:10.1175/1520-0469(1962)019<0286:TDSOTU>2.0.CO;2`.

[28] J. M. Picone, A. E. Hedin, D. P. Drob, A. C. Aikin, Nrlmsise-00 empirical model of the atmosphere: Statistical comparisons and cientific issues, Journal of Geophysical Research 107 (A12) (2002) 15–1–15–16. `doi:10.1029/2002JA009430`.

[29] O. Montenbruck, E. Gill, Satellite Orbits: Models, Methods and Applications, Springer, Berlin, 2000.

[30] M. Pilinski, Dynamic gas-surface interaction modeling for satellite aerodynamic computations, Ph.D. thesis, University of Colorado Boulder (2011).

[31] C. W. Hall, Laws and Models: Science, Engineering and Technology, 1st Edition, CRC PRess, 2018.

[32] H. Schaub, J. L. Junkins, Analytical Mechanics of Space Systems, AIAA Education Series, Reston, VA, 2014. `doi:10.2514/4.105210`.

[33] Z. Cai, M. S. de Queiroz, D. M. Dawson, A sufficiently smooth projection operator, IEEE Transactions on Automatic Control 51 (1) (2006) 135–139. `doi:10.1109/TAC.2005.861704`.

[34] H. K. Khalil, Nonlinear Systems, 3rd Edition, Prentice Hall, NJ, 2002.

Aerodynamic and Gravity Gradient based Attitude Control for CubeSats in the presence of Environmental and Spacecraft Uncertainties

Camilo Riano-Rios[a,*], Runhan Sun[a], Riccardo Bevilacqua[a], Warren E. Dixon[a]

[a] *University of Florida, 939 Sweetwater Dr., Gainesville, FL*

Abstract

In this paper, the problem of controlling the attitude of a CubeSat in low Earth orbit using only the environmental torques is considered. The CubeSat is equipped with a Drag Maneuvering Device (DMD) that enables the spacecraft to modulate its experienced aerodynamic and gravity gradient torques. An adaptive controller is designed to achieve attitude tracking of the spacecraft in the presence of uncertain parameters such as the atmospheric density, drag and lift coefficients, and the time-varying location of the Center of Mass (CoM). The proposed controller also accounts for modeling inaccuracy of the inertia matrix of the spacecraft. A Lyapunov-based analysis is used to prove that the quaternion-based attitude trajectory tracking error is uniformly ultimately bounded. The designed controller is also examined through numerical simulations for a spacecraft with time-varying uncertain drag, lift coefficients and CoM location parameters and the NRLMSISE-00 model for the atmospheric density.

Keywords: Aerodynamic Torque, Gravity Gradient Torque, Atmospheric Density, Drag, Lift, Center of Mass, Adaptive.

---

[*] Corresponding author

Email address: `crianorios@ufl.edu` (Camilo Riano-Rios)

Preprint submitted to Acta Astronautica *December 12, 2020*

1. Introduction

Missions involving small satellites in Low Earth Orbit (LEO) have become popular with the introduction of the CubeSat standard [1]. The limited volume available in these satellites has increased the need to develop propellant-less strategies for orbit and attitude control, usually exploiting the interaction of the spacecraft with the low density atmosphere [2–6]. The idea of using the drag force for relative orbit maneuvers was first introduced in [7]. Since then, a wide variety of control strategies have been developed using both aerodynamic lift and drag as the only control means [8–11]. To exploit such forces, dedicated surfaces are installed on the spacecraft to increase its area-to-mass ratio, often locating the center of pressure at distances with respect to the Center of Mass (CoM) such that significant torques can be applied. This has led to the design of CubeSats that can alter the aerodynamic torques by actively modulating the length and angle of drag surfaces. Such designs often involve several ultra-lightweight surfaces with two or more degrees of freedom [3, 4] so that the inertia matrix does not change significantly and its time derivative can be neglected in the attitude equations of motion.

The University of Florida ADvanced Autonomous MUltiple Spacecraft laboratory (ADAMUS) has designed the Drag Maneuvering Device (DMD), formerly Drag De-Orbit Device (D3) [12], and has been studying its capabilities for spacecraft controlled re-entry [13, 14], spacecraft relative maneuvering [15, 16] and attitude control [17–19] by using its four dedicated surfaces to modulate the experienced environmental forces and torques on a CubeSat. The design of the DMD provides a CubeSat with four repeatedly extendable/retractable surfaces offset 90 degrees from each other, and with 20 degrees inclination with respect to the anti-ram face of the CubeSat. The DMD has passed through several prototype iterations, and incorporates only one degree of freedom for each surface, which makes it easier to build and less susceptible to failure of moving parts. It is also capable of altering the CubeSat inertia matrix to make use of the aerodynamic and the gravity gradient torques.

Previous work in [19] presented the design of an integral concurrent learning-based control method to provide simultaneous state tracking and on-line estimation of uncertain parameters. These uncertain parameters included the average drag coefficient and atmospheric density, and the time-varying CoM location and inertia matrix were assumed known. However, in real operation, inaccurate knowledge of these two parameters could reduce the performance or even destabilize the system. Controllers that actively change the location of the CoM have been proposed for spacecraft attitude control in [20] using PID, linear quadratic regulator and partial feedback linearization techniques, and the developed control laws computed the location of the CoM so that the desired control torques can be produced. The results in [20] demonstrate how the CoM location can influence the overall performance of the system, making it necessary to account for uncertainties in this parameter. The problem of having uncertainties in the CoM location has been addressed in [21] for unmanned aerial vehicles using an adaptive controller for constant CoM. In [22], adaptive control techniques have been used to develop a propellant-based spacecraft attitude controller that considers time-dependent or input-dependent inertia parameters to account for deployable appendages or mass loss, respectively.

In this paper, the designed controller incorporates uncertainties in the CoM location and time-varying drag and lift coefficients, as well as partial knowledge of the inertia matrix of a DMD-equipped CubeSat. The cost for adding this adaptation capability is that the on-line parameter estimation feature is lost compared to [19]. However, the proposed controller provides improved robustness to uncertainties in parameters that are inaccurate and time-varying. The contribution of this paper is the design of an adaptive controller that exploits environmental torques for spacecraft attitude maneuvers in the presence of uncertainties in the time-varying CoM location, atmospheric density, drag and lift coefficients with guaranteed bounded state tracking through a Lyapunov-based stability analysis.

The remainder of this paper is organized as follows. Section 2 describes the DMD device, and Section 3 presents the spacecraft attitude dynamics. Section

4 describes the control objective and the control development. Section 5 shows the corresponding Lyapunov-based stability analysis. Sections 6 and 7 present the numerical simulation and conclusion, respectively.

2. Drag Maneuvering Device

In this paper, the controller design is based on the DMD developed in [12]. It consists of four repeatedly extendable/retractable 3.7 m long and 0.038 m width surfaces offset 90 deg and inclined 20 deg with respect to the anti-ram face of the spacecraft, as depicted in Figure 1.

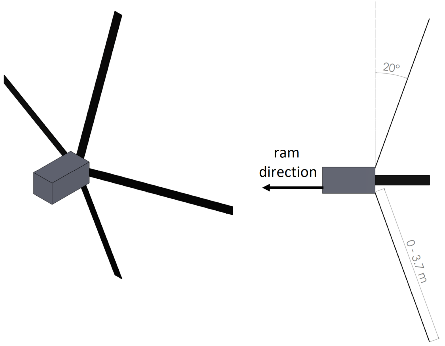

Figure 1: Drag Maneuvering Device schematic.

The surfaces are fabricated from strips of austenitic 316 stainless steel shim stock with 0.0762 mm thickness, weighting approximately 95 g. Given the weight of each boom and their lengths, significant changes in aerodynamic and gravity gradient torques can be created by independently modulating the length of each DMD surface. When the surfaces are fully extended, the DMD provides an increase of the cross-wind surface area up to 0.5 m^2.

3. Attitude Dynamics

3.1. Reference Frames

The Earth-Centered-Inertial (ECI) reference frame is considered the inertial reference frame. The orbital coordinate system is defined as: origin located at the CoM of the spacecraft. The unit vector $\boldsymbol{\hat{o}_3}$ points from the center of the Earth towards the spacecraft CoM, the unit vector $\boldsymbol{\hat{o}_2}$ is aligned with the orbit angular momentum, and the unit vector $\boldsymbol{\hat{o}_1}$ completes a right-hand Cartesian coordinate system. The body coordinate system is defined with the origin located at the CoM of the spacecraft, and the unit vectors $\boldsymbol{\hat{b}_1}$, $\boldsymbol{\hat{b}_2}$ and $\boldsymbol{\hat{b}_3}$ aligned with the longitudinal, lateral, and vertical axes of the spacecraft, respectively, as depicted in Figure 2.

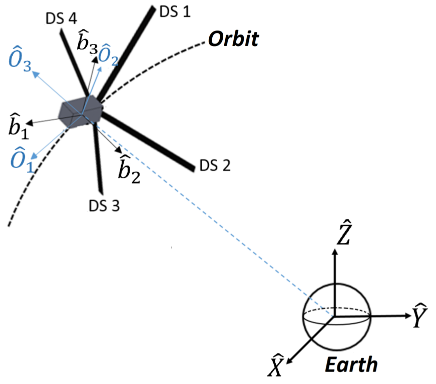

Figure 2: Coordinate systems.

3.2. Equation of Motion

The spacecraft attitude dynamics are given by

$$\dot{J}\boldsymbol{\omega} + J\dot{\boldsymbol{\omega}} + \omega^{\times} J\boldsymbol{\omega} = \boldsymbol{\tau_D} + \boldsymbol{\tau_L} + \boldsymbol{\tau_{GG}} + \boldsymbol{\delta}, \tag{1}$$

where $\boldsymbol{\omega} \in \mathbb{R}^3$ is the angular velocity of the body with respect to the inertial reference frame, $J \in \mathbb{R}^{3\times 3}$ is the inertia matrix of the spacecraft, $\boldsymbol{\tau_{GG}} \in \mathbb{R}^3$ is the gravity gradient torque, and $\boldsymbol{\tau_D}$, $\boldsymbol{\tau_L} \in \mathbb{R}^3$ are the aerodynamic torques due to drag and lift, respectively. The vector $\boldsymbol{\delta} \in \mathbb{R}^3$ denotes disturbances to the system (e.g., magnetic torques). The skew symmetric matrix $a^{\times} \in \mathbb{R}^{3\times 3}$

for a vector $\boldsymbol{a} \triangleq [a_1 \ a_2 \ a_3]^T \in \mathbb{R}^3$ is defined as

$$a^{\times} \triangleq \begin{bmatrix} 0 & -a_3 & a_2 \\ a_3 & 0 & -a_1 \\ -a_2 & a_1 & 0 \end{bmatrix}. \tag{2}$$

Remark 1. The design of the DMD considers surfaces made of austenitic stainless steel, which is considered a non-magnetic material [12]. Therefore, the DMD surfaces are not expected to generate magnetic hysteresis torques. An estimate of the maximum remaining magnetic moment of the spacecraft can be computed following the procedure in [23] under the guidelines in [24] for a class II spacecraft.

Assumption 1. The disturbance torque $\boldsymbol{\delta}$ can be upper bounded as $\|\boldsymbol{\delta}\| \leq \zeta_0$, where $\zeta_0 \in \mathbb{R}_{>0}$ is a known bounding constant. □

3.3. Quaternion Representation of the Spacecraft Orientation

The quaternion $\boldsymbol{q} \in \mathbb{R}^4$ represents the rotation of the spacecraft body with respect to an inertial frame, expressed in the body coordinate system as [25]

$$\boldsymbol{q} \triangleq \left[q_0 \ \ \boldsymbol{q_v}^T\right]^T, \tag{3}$$

where $q_0 \in \mathbb{R}$ and $\boldsymbol{q_v} = [q_1 \ q_2 \ q_3]^T \in \mathbb{R}^3$. The quaternion $\boldsymbol{q}$ has the property

$$\boldsymbol{q_v}^T \boldsymbol{q_v} + {q_0}^2 = 1. \tag{4}$$

The rotational kinematics of the spacecraft is defined as

$$\dot{\boldsymbol{q}}_{\boldsymbol{v}} \triangleq \frac{1}{2}\left(q_v^{\times} + q_0 \mathcal{I}_3\right) \boldsymbol{\omega} \tag{5}$$

$$\dot{q}_0 \triangleq -\frac{1}{2} \boldsymbol{q_v}^T \boldsymbol{\omega}, \tag{6}$$

where $\mathcal{I}_3 \in \mathbb{R}^{3\times3}$ denotes the identity matrix. To specify a desired time-varying attitude trajectory, we also define a desired quaternion $\boldsymbol{q_d} \in \mathbb{R}^4$ as

$$\boldsymbol{q_d} \triangleq \left[q_{0d} \ \ \boldsymbol{q_{vd}}^T\right]^T, \tag{7}$$

where $q_{0d} \in \mathbb{R}$ and $\boldsymbol{q_{vd}} \in \mathbb{R}^3$. Using (5) and (6), the angular velocity $\boldsymbol{\omega}$ can be expressed in terms of $\boldsymbol{q}$ as

$$\boldsymbol{\omega} = 2\left(q_0 \dot{\boldsymbol{q}}_{\boldsymbol{v}} - \boldsymbol{q_v} q_0\right) - 2q_v^{\times} \dot{\boldsymbol{q}}_{\boldsymbol{v}}, \tag{8}$$

and the desired angular velocity of the body $\boldsymbol{\omega_d}$ with respect to the inertial frame can be expressed in the desired body coordinate system as

$$\boldsymbol{\omega_d} = 2\left(q_{0d} \dot{\boldsymbol{q}}_{\boldsymbol{vd}} - \boldsymbol{q_{vd}} q_{0d}\right) - 2{q_{vd}}^{\times} \dot{\boldsymbol{q}}_{\boldsymbol{vd}}. \tag{9}$$

For simplicity, the attitude dynamics will be expressed in the body coordinate system in the subsequent stability analysis. Therefore, it is useful to define the matrices that represent the actual and desired orientation of the body with respect to the inertial frame, which are denoted by $R \in SO(3)$ and $R_d \in SO(3)$, respectively, as [25]

$$R \triangleq \left(q_0^2 - \boldsymbol{q_v}^T \boldsymbol{q_v}\right) \mathcal{I}_3 + 2\boldsymbol{q_v} \boldsymbol{q_v}^T - 2q_0 {q_v}^{\times}, \tag{10}$$

$$R_d \triangleq \left(q_{0d}^2 - \boldsymbol{q_{vd}}^T \boldsymbol{q_{vd}}\right) \mathcal{I}_3 + 2\boldsymbol{q_{vd}} \boldsymbol{q_{vd}}^T - 2q_{0d} {q_{vd}}^{\times}. \tag{11}$$

The error quaternion $\boldsymbol{e} \triangleq [e_0\ \boldsymbol{e_v}^T]^T \in \mathbb{R}^4$ that represents the mismatch between $\boldsymbol{q}$ and $\boldsymbol{q_d}$ is defined as

$$\boldsymbol{e_v} \triangleq q_{0d} \boldsymbol{q_v} - q_0 \boldsymbol{q_{vd}} + {q_v}^{\times} \boldsymbol{q_{vd}}, \tag{12}$$

$$e_0 \triangleq q_0 q_{0d} + \boldsymbol{q_v}^T \boldsymbol{q_{vd}}, \tag{13}$$

which satisfies the property

$$\boldsymbol{e_v}^T \boldsymbol{e_v} + {e_0}^2 = 1, \tag{14}$$

and obeys the error quaternion kinematics [25]

$$\dot{\boldsymbol{e}}_{\boldsymbol{v}} = \frac{1}{2}\left({e_v}^{\times} + e_0 \mathcal{I}_3\right) \tilde{\boldsymbol{\omega}}, \tag{15}$$

$$\dot{e}_0 = -\frac{1}{2} \boldsymbol{e_v}^T \tilde{\boldsymbol{\omega}}. \tag{16}$$

In (15) and (16), $\tilde{\boldsymbol{\omega}} \in \mathbb{R}^3$ denotes the error in the angular velocity of the spacecraft

$$\tilde{\boldsymbol{\omega}} \triangleq \boldsymbol{\omega} - \widetilde{R}\boldsymbol{\omega_d}, \tag{17}$$

where $\widetilde{R} \in \mathbb{R}^{3\times 3}$ is the rotation matrix used to express $\boldsymbol{\omega_d}$ in the body coordinate system, and is defined as

$$\widetilde{R} \triangleq R R_d^T = \left({e_0}^2 - {\boldsymbol{e_v}}^T \boldsymbol{e_v}\right)\mathcal{I}_3 + 2\boldsymbol{e_v}{\boldsymbol{e_v}}^T - 2e_0{e_v}^{\times}. \tag{18}$$

3.4. Aerodynamic Torques

A spacecraft in LEO experiences drag and lift forces on every surface exposed to the incoming atmosphere particles. In the case of a DMD-equipped CubeSat, the surface areas of the DMD are significantly larger than those of the body so that the latter can be neglected. The drag force $\boldsymbol{F_{D,j}} \in \mathbb{R}^3$ and the lift force $\boldsymbol{F_{L,j}} \in \mathbb{R}^3$ are assumed to act on the geometric center of each DMD surface and can be expressed as

$$\boldsymbol{F_{D,j}} = -\frac{\rho w_b L_j C_{D,j}}{2}\|\boldsymbol{V}_{\perp,j}\|^2 \frac{\boldsymbol{V_r}}{\|\boldsymbol{V_r}\|} \tag{19}$$

and

$$\boldsymbol{F_{L,j}} = -\frac{\rho w_b L_j C_{L,j}}{2}\|\boldsymbol{V}_{\perp,j}\|^2 \left(\frac{\boldsymbol{V_r}}{\|\boldsymbol{V_r}\|} \times \boldsymbol{n_j} \times \frac{\boldsymbol{V_r}}{\|\boldsymbol{V_r}\|}\right). \tag{20}$$

In (19) and (20), the subscript j indicates the j^{th} DMD surface, $\rho \in \mathbb{R}$ is the atmospheric density, $C_{D,j}$, $C_{L,j}$, w_b, $L_j \in \mathbb{R}$ are drag and lift coefficients, and the width and length of the corresponding DMD surface, respectively. The spacecraft-atmosphere relative velocity vector $\boldsymbol{V_r} \in \mathbb{R}^3$, assuming that the atmosphere co-rotates with the Earth, is defined as

$$\boldsymbol{V_r} \triangleq \dot{\boldsymbol{R}}_{\boldsymbol{c}} - \boldsymbol{\omega}_{\oplus} \times \boldsymbol{R_c}, \tag{21}$$

where $\boldsymbol{\omega}_{\oplus} \in \mathbb{R}^3$ is the angular velocity of the Earth, and $\boldsymbol{R_c}, \dot{\boldsymbol{R}}_{\boldsymbol{c}} \in \mathbb{R}^3$ represent the ECI position and velocity of the spacecraft, respectively. The vector $n_j \in \mathbb{R}^3$

is a unit vector that represents the direction normal to the j^{th} DMD surface and $\boldsymbol{V_{\perp,j}} \triangleq \boldsymbol{V_r}\cdot\boldsymbol{n_j}$.

Remark 2. Density models with different levels of accuracy have been developed throughout the years. The U.S Standard [26] and Harris-Priester [27] models are altitude-based theoretical models that provide values for the atmospheric density based on the spacecraft altitude at a low computational cost. More accurate and complex models, such as the NRLMSISE-00 [28] also incorporate data gathered from real missions to provide atmospheric density values dependent on the date, time, spacecraft position as well as solar and geomagnetic indices. However, more complex density models require significantly higher computational effort and forecasts of solar and geomagnetic activity that are affected by additional uncertainties. Given the multiple sources of uncertainty and approximations in the density models, the error is still significant even with the most accurate ones [29].

The subsequent development is based on the analytical models for drag and lift coefficients presented in [30] that assume flat plates in a free molecular flow as

$$\begin{aligned} C_{D,j} \triangleq\ & \frac{2}{s\sqrt{\pi}}\exp(-s^2\sin^2(\theta_{in})) \\ & + \frac{\sin(\theta_{in})}{s^2}(1+2s^2)\operatorname{erf}(s\sin(\theta_{in})) + \frac{\sqrt{\pi}}{s}\sin^2(\theta_{in})\sqrt{T_{k,out}/T_a} \end{aligned} \tag{22}$$

$$C_{L,j} \triangleq \frac{\cos(\theta_{in})}{s^2}\operatorname{erf}(s\cos(\theta_{in})) + \frac{1}{s}\sqrt{\pi}\cos(\theta_{in})\sin(\theta_{in})\sqrt{T_{k,out}/T_a}, \tag{23}$$

where $\operatorname{erf}(\cdot)$ represents the error function [31], $s \triangleq \|\boldsymbol{V_r}\|\sqrt{m/(2k_BT_a)} \in \mathbb{R}$ is an auxiliary variable, $m \in \mathbb{R}$ is the mass of the spacecraft, $k_B \in \mathbb{R}$ is the Boltzmann constant, $\theta_{in} \in \mathbb{R}$ is the principal rotation angle between $\boldsymbol{V_r}$ and $\boldsymbol{n_j}$, and $T_a \in \mathbb{R}$ is the ambient atmosphere temperature. The kinetic temperature of reflected particles at the surface $T_{k,out} \in \mathbb{R}$ is defined as

$$T_{k,out} \triangleq \frac{m}{3k_B}\|\boldsymbol{V}_r\|^2(1-\alpha) + \alpha T_s, \tag{24}$$

where $T_s \in \mathbb{R}$ is the temperature of the surface, and $\alpha \in \mathbb{R}$ is an accommodation coefficient that represents the influence of the surface material properties.

The torques produced by aerodynamic drag and lift are given by

$$\boldsymbol{\tau_k} \triangleq \sum_{j=1}^{4} R_j{}^{\times} \boldsymbol{F_{k,j}}, \quad k = D, L, \tag{25}$$

where $\boldsymbol{R_j} \triangleq \boldsymbol{r_c} + \boldsymbol{r_j}$, $\boldsymbol{r_c} \triangleq [c_1 \ c_2 \ c_3]^T \in \mathbb{R}^3$ is the uncertain vector that goes from the spacecraft CoM to the geometric center of the rear face of the CubeSat (O'), and $\boldsymbol{r_j} \in \mathbb{R}^3$ is the vector that goes from O' to the center of pressure of the j^{th} DMD surface. Given the geometry and capabilities of the DMD, the vector $\boldsymbol{r_c}$ also varies with the level of deployment of the drag surfaces.

3.5. Gravity Gradient Torque

The DMD-equipped CubeSat, considered a rigid body in space, experiences a gradient of gravitational force along the body with the greatest attraction on the parts that are closer to the Earth. This gradient produces the so-called Gravity Gradient Torque (GGT) that depends on the attitude and inertia properties. The GGT is given by [32]

$$\boldsymbol{\tau_{GG}} \triangleq \frac{3GM_{\oplus}}{\|\boldsymbol{R}_c\|^5} R_c{}^{\times} J \boldsymbol{R_c}, \tag{26}$$

where $M_{\oplus} \in \mathbb{R}_{>0}$ is the mass of the Earth, and $G \in \mathbb{R}_{>0}$ is the universal gravitational constant.

The GGT can be changed by extending/retracting the DMD surfaces which directly affect the inertia matrix. A simple model to compute the variation of the inertia matrix by assuming DMD surfaces that can be divided as a thick walled cylinder (rolled portion) and a flat plate (deployed portion) [17], is used to propagate the attitude dynamics for the numerical simulation in Section 6.

4. Control Design

4.1. Control Objective

The objective is to design an adaptive controller for the spacecraft attitude to track a given time-varying reference $\boldsymbol{q_d}$ using only the influence of environmental torques on the spacecraft attitude dynamics as described in (1). Uncertainties associated with the average atmospheric density ρ and drag coefficient C_D have been addressed in previous work from the authors in [19]. However, assumptions such as perfect knowledge of the inertia matrix J and the location of the CoM $\boldsymbol{r_c}$ were made to achieve the control objective along with on-line parameter estimation. In this work, at the cost of losing the on-line parameter estimation feature, an augmented vector is proposed to compensate for the uncertainties.

Although analytical models to compute the variation of the inertia matrix can be developed, modeling approximations are inherent and lead to uncertain disturbances. Moreover, modeling deviations in the CoM location will also result in inaccurately computing levels of deployment for the DMD surfaces to produce the torques required by a designed control law.

To achieve the proposed control objective, the subsequent control design will be performed under the following assumptions.

Assumption 2. The spacecraft has the capability of using the computationally light Harris-Priester model [27] to calculate the atmospheric density $\rho_{HP} \in \mathbb{R}_{>0}$ on-board. The real atmospheric density, whose behavior is more complex than what is captured by the Harris-Priester model, is assumed to be approximated by

$$\rho \triangleq B_1 + B_2\ \rho_{HP}, \tag{27}$$

where $B_1,\ B_2 \in \mathbb{R}$ are unknown calibration constants. □

Assumption 3. The spacecraft is capable of approximately computing its time-varying inertia matrix $J_m \in \mathbb{R}^{3\times3}$, provided an on-board simplified analytical model. The actual inertia matrix J can be expressed as

$$J = J_m + \Delta J, \tag{28}$$

where $\Delta J \in \mathbb{R}^{3\times 3}$ is the mismatch between the actual and modeled inertia matrix. The inertia mismatch ΔJ, as well as its time derivative $\Delta\dot{J}$, are assumed bounded by known constants. Moreover, since the DMD surfaces are driven by motors with limited velocity, then the rate of change of the inertia matrix $\dot{J}$ can also be bounded by a known constant. □

Assumption 4. The desired quaternion $\boldsymbol{q_d}$, desired angular velocity $\boldsymbol{\omega_d}$ and its time derivative $\dot{\boldsymbol{\omega}}_{\boldsymbol{d}}$ are known and bounded signals such that

$$\|\boldsymbol{q_d}\| \leq \zeta_1,\ \|\boldsymbol{\omega_d}\| \leq \zeta_2,\ \|\dot{\boldsymbol{\omega}}_{\boldsymbol{d}}\| \leq \zeta_3, \tag{29}$$

where $\zeta_1,\ \zeta_2,\ \zeta_3 \in \mathbb{R}_{>0}$ are known bounding constants. □

Assumption 5. The spacecraft is equipped with an attitude determination system that provides the controller with measurements of the angular velocity $\boldsymbol{\omega}$ and quaternion $\boldsymbol{q}$. □

Since the components of $\boldsymbol{e}$ satisfy (14), the attitude control objective can be established as

$$\widetilde{R} \rightarrow \mathcal{I}_3 \quad \text{as} \quad t \rightarrow \infty. \tag{30}$$

Based on (12)-(14), the control objective in (30) can be achieved if

$$\|\boldsymbol{e_v}\| \rightarrow 0 \Rightarrow |\, e_0 \,| \rightarrow 1. \tag{31}$$

4.2. Control Development

Let the modified state vector $\boldsymbol{r} \in \mathbb{R}^3$ be defined as

$$\boldsymbol{r} \triangleq \tilde{\boldsymbol{\omega}} + \beta \boldsymbol{e_v}, \tag{32}$$

where $\beta \in \mathbb{R}^{3\times 3}$ is a symmetric, positive-definite control gain matrix. Taking the time derivative of $\boldsymbol{r}$ and pre-multiplying by the inertia matrix J yields

$$J\dot{\boldsymbol{r}} = \boldsymbol{\tau_D} + \boldsymbol{\tau_L} + \frac{3GM_\oplus}{\|\boldsymbol{R_c}\|^5} {R_c}^\times J \boldsymbol{R_c} + \boldsymbol{\delta} - \dot{J}\boldsymbol{\omega} - \omega^\times J \boldsymbol{\omega} - J\dot{\widetilde{R}}\boldsymbol{\omega_d} - J\widetilde{R}\dot{\boldsymbol{\omega}}_{\boldsymbol{d}} + J\beta\dot{\boldsymbol{e}}_{\boldsymbol{v}}. \tag{33}$$

Using (15), (17), Assumption 3 and the fact that $\dot{\widetilde{R}} = -\omega^{\times}\widetilde{R}$ yields

$$J\dot{\boldsymbol{r}} = \boldsymbol{f} + \widetilde{\boldsymbol{N}} + \boldsymbol{N_B}, \tag{34}$$

where $\boldsymbol{f}, \widetilde{\boldsymbol{N}}, \boldsymbol{N_B} \in \mathbb{R}^3$ are auxiliary variables defined as

$$\begin{aligned} \boldsymbol{f} \triangleq\ & \boldsymbol{\tau_D} + \boldsymbol{\tau_L} + \frac{3GM_{\oplus}}{\|\boldsymbol{R_c}\|^5} R_c{}^{\times} J_m \boldsymbol{R_c} - \dot{J}_m \boldsymbol{\omega} \\ & - \omega^{\times} J_m \boldsymbol{\omega} + J_m \omega^{\times} \widetilde{R} \boldsymbol{\omega_d} - J_m \widetilde{R} \dot{\boldsymbol{\omega}}_{\boldsymbol{d}} + J_m \beta \dot{\boldsymbol{e}}_{\boldsymbol{v}}, \end{aligned} \tag{35}$$

$$\begin{aligned} \widetilde{\boldsymbol{N}} \triangleq\ & -\Delta\dot{J}\tilde{\boldsymbol{\omega}} - \tilde{\omega}^{\times}\Delta J\left(\tilde{\boldsymbol{\omega}} + \widetilde{R}\boldsymbol{\omega_d}\right) - \left(\widetilde{R}\boldsymbol{\omega_d}\right)^{\times} \Delta J \tilde{\boldsymbol{\omega}} \\ & + \Delta J \tilde{\omega}^{\times} \widetilde{R} \boldsymbol{\omega_d} + \frac{1}{2}\Delta J \beta \left(e_v{}^{\times} + e_0 \mathcal{I}_3\right) \tilde{\boldsymbol{\omega}}, \end{aligned} \tag{36}$$

$$\boldsymbol{N_B} \triangleq -\Delta\dot{J}\widetilde{R}\boldsymbol{\omega_d} - \left(\widetilde{R}\boldsymbol{\omega_d}\right)^{\times} \Delta J \widetilde{R}\boldsymbol{\omega_d} + \frac{3GM_{\oplus}}{\|\boldsymbol{R_c}\|^5} R_c{}^{\times} \Delta J \boldsymbol{R_c} + \boldsymbol{\delta} - \Delta J \widetilde{R} \dot{\boldsymbol{\omega}}_{\boldsymbol{d}}. \tag{37}$$

Since $\tilde{\boldsymbol{\omega}} = \boldsymbol{r} - \beta \boldsymbol{e_v}$, and considering that $\|\boldsymbol{R_c}\|$ can be upper bounded by a known constant. Using Assumptions 3 and 4, $\widetilde{\boldsymbol{N}}$ and $\boldsymbol{N_B}$ can be upper bounded as

$$\|\widetilde{\boldsymbol{N}}\| \leq \sigma\left(\|\boldsymbol{\eta}\|\right)\|\boldsymbol{\eta}\|, \tag{38}$$

$$\|\boldsymbol{N_B}\| \leq \zeta_4, \tag{39}$$

where $\zeta_4 \in \mathbb{R}_{>0}$ is a known bounding constant, $\boldsymbol{\eta} \in \mathbb{R}^6$ is an augmented state vector defined as

$$\boldsymbol{\eta} \triangleq \left[\boldsymbol{e_v}^T\ \boldsymbol{r}^T\right]^T, \tag{40}$$

and $\sigma : \mathbb{R}^6 \to \mathbb{R}$ is a positive, globally invertible and non-decreasing function.

To include the adaptation capabilities that compensate for the unknown parameters, the term $\boldsymbol{f}$ that contains only measurable states and the modeled inertia matrix J_m, can be linearly parameterized with respect to the unknown parameters. First, consider the contribution of the j^{th} DMD surface to the force due to the aerodynamic drag and lift $\boldsymbol{F_{AT,j}} \in \mathbb{R}^3$ which can be expressed using Assumption 2 as

$$\boldsymbol{F_{AT,j}} \triangleq Y_j \boldsymbol{\Theta_j}, \qquad j = 1, 2, 3, 4. \tag{41}$$

In (41) $Y_j \in \mathbb{R}^{3\times 4}$ are measurable regression matrices defined as

$$Y_j \triangleq \\ \left[-\frac{L_j w_b \|\boldsymbol{V_{\perp,j}}\|^2}{2\|\boldsymbol{V_r}\|} \boldsymbol{V_r} \left[1 \;\, \rho_{HP}\right] \quad -\frac{L_j w_b \|\boldsymbol{V}_{\perp,j}\|^2}{2} \left(\frac{\boldsymbol{V_r}}{\|\boldsymbol{V_r}\|} \times \boldsymbol{n_j} \times \frac{\boldsymbol{V_r}}{\|\boldsymbol{V_r}\|} \right) \left[1 \;\, \rho_{HP}\right] \right] \tag{42}$$

and the vectors $\boldsymbol{\Theta_j} \in \mathbb{R}^4$ are

$$\boldsymbol{\Theta_j} \triangleq \begin{bmatrix} B_1 C_{D,j} & B_2 C_{D,j} & B_1 C_{L,j} & B_2 C_{L,j} \end{bmatrix}^T. \tag{43}$$

Therefore, the total aerodynamic torque $\boldsymbol{\tau_{AT,j}} \in \mathbb{R}^3$ due to the aerodynamic drag and lift in (25) can be rewritten as

$$\boldsymbol{\tau_{AT}} \triangleq \boldsymbol{\tau_D} + \boldsymbol{\tau_L} = {r_c}^{\times} \sum_{j=1}^{4} \left(Y_j \boldsymbol{\Theta_j} \right) + \sum_{j=1}^{4} \left({r_j}^{\times} Y_j \boldsymbol{\Theta_j} \right). \tag{44}$$

In (44), the first term can be expressed as

$${r_c}^{\times} \sum_{j=1}^{4} \left(Y_j \boldsymbol{\Theta_j} \right) = \begin{bmatrix} \mathbf{0}_{1\times 16} & Y_r(3) & -Y_r(2) \\ -Y_r(3) & \mathbf{0}_{1\times 16} & Y_r(1) \\ Y_r(2) & -Y_r(1) & \mathbf{0}_{1\times 16} \end{bmatrix} \begin{bmatrix} \boldsymbol{\Theta_r} c_1 \\ \boldsymbol{\Theta_r} c_2 \\ \boldsymbol{\Theta_r} c_3 \end{bmatrix}, \tag{45}$$

where $Y_r \in \mathbb{R}^{3\times 16}$ is a measurable regression matrix defined as

$$Y_r \triangleq \begin{bmatrix} Y_1 & Y_2 & Y_3 & Y_4 \end{bmatrix}, \tag{46}$$

and $Y_r(k)$ denotes the k^{th} row of Y_r. Similarly, the vector of uncertain parameters $\boldsymbol{\Theta_r} \in \mathbb{R}^{16}$ is defined as

$$\boldsymbol{\Theta_r} \triangleq \begin{bmatrix} \boldsymbol{\Theta_1}^T \; \boldsymbol{\Theta_2}^T \; \boldsymbol{\Theta_3}^T \; \boldsymbol{\Theta_4}^T \end{bmatrix}^T. \tag{47}$$

The second term in (44) can be expressed as

$$\sum_{j=1}^{4}\left(r_j{}^{\times} Y_j \boldsymbol{\Theta_j}\right) = \sum_{j=1}^{4}\left(\begin{bmatrix} Y_j(3)r_{j,2} - Y_j(2)r_{j,3} \\ Y_j(1)r_{j,3} - Y_j(3)r_{j,1} \\ Y_j(2)r_{j,1} - Y_j(1)r_{j,2} \end{bmatrix} \boldsymbol{\Theta_j}\right), \tag{48}$$

where $\boldsymbol{r_j} \triangleq [r_{j,1}\ r_{j,2}\ r_{j,3}]^T$ is the vector defined in (25), and $Y_j(k)$ denotes the k^{th} row of Y_j. Substituting (45) and (48) into (44) yields

$$\boldsymbol{\tau_{AT}} = Y_{AT}\boldsymbol{\Theta_{AT}}, \tag{49}$$

where $Y_{AT} \in \mathbb{R}^{3\times 64}$ is a measurable regression matrix and $\boldsymbol{\Theta_{AT}} \in \mathbb{R}^{64}$ is a vector of uncertain parameters, and are defined as

$$Y_{AT} =$$

$$\begin{bmatrix} \mathbf{0}_{1\times 16} & Y_r(3) & -Y_r(2) & Y_1(3)r_{1,2} - Y_1(2)r_{1,3} & \cdots & Y_4(3)r_{4,2} - Y_4(2)r_{4,3} \\ -Y_r(3) & \mathbf{0}_{1\times 16} & Y_r(1) & Y_1(1)r_{1,3} - Y_1(3)r_{1,1} & \cdots & Y_4(1)r_{4,3} - Y_4(3)r_{4,1} \\ Y_r(2) & -Y_r(1) & \mathbf{0}_{1\times 16} & Y_1(2)r_{1,1} - Y_1(1)r_{1,2} & \cdots & Y_4(2)r_{4,1} - Y_4(1)r_{4,2} \end{bmatrix}, \tag{50}$$

$$\boldsymbol{\Theta_{AT}} = \left[\boldsymbol{\Theta_r}{}^T c_1 \quad \boldsymbol{\Theta_r}{}^T c_2 \quad \boldsymbol{\Theta_r}{}^T c_3 \quad \boldsymbol{\Theta_r}{}^T\right]^T, \tag{51}$$

respectively. Therefore, (35) can be rewritten as

$$\boldsymbol{f} = Y\boldsymbol{\Theta}, \tag{52}$$

where $Y \triangleq \Big[Y_{AT} \quad \frac{3GM_{\oplus}}{\|\boldsymbol{R_c}\|^5} R_c^{\times} J_m \boldsymbol{R_c} - \dot{J}_m \boldsymbol{\omega} - \omega^{\times} J_m \boldsymbol{\omega} + J_m \omega^{\times} \widetilde{R}\boldsymbol{\omega_d} - J_m \widetilde{R}\dot{\boldsymbol{\omega}}_{\boldsymbol{d}} + J_m \beta \dot{\boldsymbol{e}}_{\boldsymbol{v}}\Big] \in \mathbb{R}^{3\times 65}$ is the measurable augmented regression matrix, and $\boldsymbol{\Theta} \triangleq \left[\boldsymbol{\Theta_{AT}}{}^T\ 1\right]^T \in \mathbb{R}^{65}$ is the augmented vector of uncertain parameters.

Assumption 6. The time-varying vector of uncertain parameters $\boldsymbol{\Theta}$ and its time derivative, i.e., $\dot{\boldsymbol{\Theta}}$, are bounded by known constants. The bounds for $\boldsymbol{\Theta}$ are given by

$$\underline{\boldsymbol{\Theta}} \le \boldsymbol{\Theta} \le \overline{\boldsymbol{\Theta}}, \tag{53}$$

where $\underline{\boldsymbol{\Theta}}, \overline{\boldsymbol{\Theta}} \in \mathbb{R}^{65}$ are constant vectors containing the lower and upper bounds of $\boldsymbol{\Theta}$, respectively. □

Define the estimation error $\widetilde{\boldsymbol{\Theta}} \in \mathbb{R}^{65}$ as

$$\widetilde{\boldsymbol{\Theta}} = \boldsymbol{\Theta} - \widehat{\boldsymbol{\Theta}}, \tag{54}$$

where $\widehat{\boldsymbol{\Theta}} \in \mathbb{R}^{65}$ is the estimate of $\boldsymbol{\Theta}$. Using (52) and (54), and adding and subtracting the term $Y\widehat{\boldsymbol{\Theta}}$ to the open-loop error system in (34) yields

$$J\dot{\boldsymbol{r}} = Y\widetilde{\boldsymbol{\Theta}} + Y\widehat{\boldsymbol{\Theta}} + \widetilde{\boldsymbol{N}} + \boldsymbol{N_B}. \tag{55}$$

The regression matrix Y contains measurable states and is influenced by the actual inputs (i.e., the DMD surfaces lengths $L_1,\ L_2,\ L_3,\ L_4$), while the update law for the estimated vector $\widehat{\boldsymbol{\Theta}}$ will be subsequently designed. Therefore, the measurable product $Y\widehat{\boldsymbol{\Theta}}$ can be altered by modulating the length of the DMD surfaces. This term is designated as the auxiliary control input $\bar{\boldsymbol{u}} \in \mathbb{R}^3$

$$Y\widehat{\boldsymbol{\Theta}} \triangleq \bar{\boldsymbol{u}}. \tag{56}$$

To facilitate the subsequent stability analysis, let the desired auxiliary control signal $\bar{\boldsymbol{u}}_{\boldsymbol{d}} \in \mathbb{R}^3$ be designed as

$$\bar{\boldsymbol{u}}_{\boldsymbol{d}} \triangleq -K_1\boldsymbol{r} - \beta_1\boldsymbol{e_v}, \tag{57}$$

where $\beta_1 \in \mathbb{R}_{>0}$ is a positive constant gain, and $K_1 \in \mathbb{R}^{3\times3}$ is a constant, positive-definite control gain matrix. Adding and subtracting $\bar{\boldsymbol{u}}_{\boldsymbol{d}}$ and substituting (56) and (57) into (55) yields the closed-loop error system

$$J\dot{\boldsymbol{r}} = Y\widetilde{\boldsymbol{\Theta}} + \widetilde{\boldsymbol{N}} + \boldsymbol{N_B} + \boldsymbol{\chi} - K_1\boldsymbol{r} - \beta_1\boldsymbol{e_v}, \tag{58}$$

where $\boldsymbol{\chi} \triangleq \bar{\boldsymbol{u}} - \bar{\boldsymbol{u}}_{\boldsymbol{d}} \in \mathbb{R}^3$ represents the mismatch between the desired and the actual auxiliary control inputs. Based on (58), the gradient-based adaptation law is designed as

$$\dot{\widehat{\boldsymbol{\Theta}}} \triangleq \operatorname{proj}(\Gamma Y^T\boldsymbol{r}), \tag{59}$$

where $\Gamma \in \mathbb{R}^{65\times 65}$ is a constant, positive-definite adaptation gain matrix, and $\mathrm{proj}(\cdot)$ denotes the continuous projection algorithm presented in [33]. Based on the value of $(\cdot)$ and the known bounds of $\widehat{\boldsymbol{\Theta}}$, the design in $\dot{\widehat{\boldsymbol{\Theta}}}$ ensures $\widehat{\boldsymbol{\Theta}}$ remains within the known bounded region without altering the stability of the system nor introducing undesired discontinuities.

5. Stability Analysis

To facilitate the stability analysis, some definitions are introduced. Let $\lambda_1,\ \lambda_2,\ \lambda_3,\ \lambda_4 \in \mathbb{R}_{>0}$ be defined as $\lambda_1 \triangleq \lambda_{\min}\{K_1\} - \zeta_5 - 1$, $\lambda_2 \triangleq \beta_1 \lambda_{\min}\{\beta\}$, $\lambda_3 \triangleq \min\left(\lambda_1, \lambda_2\right)$, and $\lambda_4 \triangleq \lambda_3 - \frac{\sigma^2(\|\boldsymbol{\eta}\|)}{2}$, respectively, where β is the control gain defined in (32), $K_1,\ \beta_1$ are the control gains used in (57), $\sigma\left(\|\boldsymbol{\eta}\|\right)$ is the function defined in (38), $\zeta_5 \in \mathbb{R}_{>0}$ is a known bounding constant, and $\lambda_{\min}\{\cdot\} \in \mathbb{R}$ is the minimum eigenvalue of $\{\cdot\}$. Let the set $\mathcal{D}$ be defined as $\mathcal{D} \triangleq \left\{\boldsymbol{\eta} \,\middle|\, \|\boldsymbol{\eta}\| < \sigma^{-1}\left(\sqrt{2\lambda_3}\right)\right\}$, and let $\mathcal{S} \subset \mathcal{D}$ be defined as

$$\mathcal{S} \triangleq \left\{\boldsymbol{\eta} \in \mathcal{D} \,\middle|\, \|\boldsymbol{\eta}\| < \Lambda\right\}, \tag{60}$$

where $\Lambda \triangleq \sqrt{\frac{\underline{\lambda}}{\bar{\lambda}}\left(\sigma^{-1}\left(\sqrt{2\lambda_3}\right)\right)^2 - \frac{\bar{\zeta}-\underline{\zeta}}{\bar{\lambda}}}$, and $\underline{\lambda},\ \bar{\lambda},\ \underline{\zeta},\ \bar{\zeta} \in \mathbb{R}_{>0}$ are known bounding constants.

Theorem. Consider the spacecraft attitude dynamics governed by the nonlinear system in (1) with Assumptions 1-5. The auxiliary controller in (57) and the adaptive update law in (59) ensure uniformly ultimately bounded attitude tracking in the sense that

$$\|\boldsymbol{e_v}\| \leq \epsilon_1 \exp\left\{-\epsilon_2 t\right\} + \epsilon_3, \tag{61}$$

where $\epsilon_1 \triangleq \sqrt{\frac{\bar{\lambda}\|\boldsymbol{\eta}(0)\|^2 + \bar{\zeta}}{\underline{\lambda}}} \in \mathbb{R}_{>0}$, $\epsilon_2 \triangleq \frac{\lambda_4}{2\bar{\lambda}} \in \mathbb{R}_{>0}$, $\epsilon_3 \triangleq \sqrt{\frac{\bar{\lambda}}{\lambda_4 \underline{\lambda}}\zeta_8 + \frac{\bar{\zeta}-\underline{\zeta}}{\underline{\lambda}}} \in \mathbb{R}_{>0}$, $\zeta_8 \triangleq \zeta_6 + \frac{(\zeta_4+\zeta_7)^2}{2} \in \mathbb{R}_{>0}$, and $\zeta_6,\ \zeta_7 \in \mathbb{R}_{>0}$ are known bounding constants. Provided that $\boldsymbol{\eta}(0) \in \mathcal{S}$ is satisfied, and that the control gains are selected sufficiently large such that $\lambda_1 > 0$, and $\Lambda > \epsilon_3$.

Proof. Let $V \in \mathbb{R}_{\geq 0}$ be a candidate Lyapunov function defined as

$$V(t) \triangleq \frac{1}{2}\boldsymbol{r}^T J \boldsymbol{r} + \beta_1 \boldsymbol{e_v}^{\boldsymbol{T}} \boldsymbol{e_v} + \beta_1 (1 - e_0)^2 + \frac{1}{2}\widetilde{\boldsymbol{\Theta}}^T \Gamma^{-1} \widetilde{\boldsymbol{\Theta}}. \tag{62}$$

The Lypaunov function can be upper and lower bounded as

$$\underline{\lambda}\|\boldsymbol{\eta}\|^2+\underline{\zeta} \leq V(t) \leq \bar{\lambda}\|\boldsymbol{\eta}\|^2+\bar{\zeta}. \tag{63}$$

Substituting (15), (16), (32), (54) and (58) into the time derivative of (62), and using the fact that $\boldsymbol{e_v}^T e_v{}^{\times}\tilde{\boldsymbol{\omega}} = 0$, yields

$$\begin{aligned}\dot{V}(t) = \boldsymbol{r}^T\left(Y\widetilde{\boldsymbol{\Theta}} + \widetilde{\boldsymbol{N}} + \boldsymbol{N_B} + \boldsymbol{\chi} - K_1\boldsymbol{r}\right) + \frac{1}{2}\boldsymbol{r}^T\dot{J}\boldsymbol{r} \\ - \beta_1\boldsymbol{e_v}^T\beta\boldsymbol{e_v} + \widetilde{\boldsymbol{\Theta}}^T\Gamma^{-1}\dot{\boldsymbol{\Theta}} - \widetilde{\boldsymbol{\Theta}}^T\Gamma^{-1}\dot{\hat{\boldsymbol{\Theta}}}.\end{aligned} \tag{64}$$

Substituting the adaptive update law in (59) into (64), yields

$$\dot{V}(t) = \boldsymbol{r}^T\widetilde{\boldsymbol{N}} + \boldsymbol{r}^T\boldsymbol{N_B} + \boldsymbol{r^T}\boldsymbol{\chi} - \boldsymbol{r}^T K_1\boldsymbol{r} - \beta_1\boldsymbol{e_v}^T\beta\boldsymbol{e_v} + \frac{1}{2}\boldsymbol{r}^T\dot{J}\boldsymbol{r} + \widetilde{\boldsymbol{\Theta}}^T\Gamma^{-1}\dot{\boldsymbol{\Theta}}. \tag{65}$$

In (64), the last two terms can be upper bounded using Assumptions 3 and 6 as

$$\frac{1}{2}\boldsymbol{r}^T\dot{J}\boldsymbol{r} \leq \zeta_5\|\boldsymbol{r}\|^2, \tag{66}$$

$$\widetilde{\boldsymbol{\Theta}}^T\Gamma^{-1}\dot{\boldsymbol{\Theta}} \leq \zeta_6. \tag{67}$$

Using (38), (39), (66) and (67), (65) can be upper bounded as

$$\begin{aligned}\dot{V}(t) \leq & -\left(\lambda_{\min}\{K_1\} - \zeta_5\right)\|\boldsymbol{r}\|^2 \\ & - \beta_1\lambda_{\min}\{\beta\}\|\boldsymbol{e_v}\|^2 + \sigma(\|\boldsymbol{\eta}\|)\|\boldsymbol{\eta}\|\|\boldsymbol{r}\| + \left(\zeta_4 + \|\boldsymbol{\chi}\|\right)\|\boldsymbol{r}\| + \zeta_6.\end{aligned} \tag{68}$$

Assumption 7. A numerical optimization algorithm can be used to find a suitable set of DMD surface lengths (i.e., L_1, L_2, L_3 and L_4) that minimizes $\|\boldsymbol{\chi}\|$, and the resulting $\boldsymbol{\chi}$ can be upper bounded by a constant for the entire maneuver such that $\|\boldsymbol{\chi}\| \leq \zeta_7$. □

Using Young's inequality on the term $\sigma(\|\boldsymbol{\eta}\|)\|\boldsymbol{\eta}\|\|\boldsymbol{r}\|$ yields $\sigma(\|\boldsymbol{\eta}\|)\|\boldsymbol{\eta}\|\|\boldsymbol{r}\| \leq \frac{\sigma^2(\|\boldsymbol{\eta}\|)\|\boldsymbol{\eta}\|^2}{2} + \frac{1}{2}\|\boldsymbol{r}\|^2$. Similarly, the inequality $\left(\zeta_4 + \|\boldsymbol{\chi}\|\right)\|\boldsymbol{r}\| \leq \frac{1}{2}\|\boldsymbol{r}\|^2 + \frac{(\zeta_4+\zeta_7)^2}{2}$ can be obtained using Assumption 7. Therefore, (68) can be rewritten as

$$\dot{V}(t) \leq -\lambda_1\|\boldsymbol{r}\|^2 - \lambda_2\|\boldsymbol{e_v}\|^2 + \frac{\sigma^2(\|\boldsymbol{\eta}\|)\|\boldsymbol{\eta}\|^2}{2} + \zeta_8. \tag{69}$$

The expression in (69) can be further upper bounded as

$$\dot{V}(t) \leq -\left(\lambda_3 - \frac{\sigma^2(\|\boldsymbol{\eta}\|)}{2}\right)\|\boldsymbol{\eta}\|^2 + \zeta_8. \tag{70}$$

Provided $\boldsymbol{\eta} \in \mathcal{D}$, then (70) can be rewritten as

$$\dot{V}(t) \leq -\lambda_4\|\boldsymbol{\eta}\|^2 + \zeta_8 \quad \forall \boldsymbol{\eta} \in \mathcal{D}. \tag{71}$$

Using the bounds in (63), (71) can be rewritten as

$$\dot{V}(t) \leq -\frac{\lambda_4}{\overline{\lambda}}V(t) + \epsilon_0, \tag{72}$$

where $\epsilon_0 \triangleq \zeta_8 + \frac{\lambda_4\overline{\zeta}}{\overline{\lambda}}$. By invoking the Comparison Lemma from [34], the solution to (72) can be obtained as

$$V(t) \leq \exp\left\{-\frac{\lambda_4}{\overline{\lambda}}t\right\}V(0) + \frac{\overline{\lambda}}{\lambda_4}\epsilon_0\left(1 - \exp\left\{-\frac{\lambda_4}{\overline{\lambda}}t\right\}\right). \tag{73}$$

Using (63) and (73) yields

$$\|\boldsymbol{\eta}\|^2 \leq \left(\frac{\overline{\lambda}\|\boldsymbol{\eta}(0)\|^2 + \overline{\zeta}}{\underline{\lambda}}\right)\exp\left\{-\frac{\lambda_4}{\overline{\lambda}}t\right\} + \left(\frac{\overline{\lambda}}{\lambda_4\underline{\lambda}}\zeta_8 + \frac{\overline{\zeta} - \underline{\zeta}}{\underline{\lambda}}\right). \tag{74}$$

Using (40) and (74) yields the uniformly ultimately bounded result in (61) provided $\boldsymbol{\eta}(0) \in \mathcal{S}$, where uniformity in initial time can be concluded from the independence of λ_3 and the ultimate bound from ϵ_3 at time $t = 0$. From (62), (63) and (73), then $\boldsymbol{r} \in \mathcal{L}_\infty$. Then, from (17) and (32), $\boldsymbol{\omega} \in \mathcal{L}_\infty$. Similarly, from (15) and (16), $\dot{\boldsymbol{e}}_{\boldsymbol{v}}$, $\dot{e}_0 \in \mathcal{L}_\infty$. Since $\boldsymbol{r}$, $\boldsymbol{\omega} \in \mathcal{L}_\infty$, and $\boldsymbol{e}_v$, e_0, $\boldsymbol{\omega}_{\boldsymbol{d}} \in \mathcal{L}_\infty$ by definition, then $\bar{\boldsymbol{u}}_{\boldsymbol{d}} \in \mathcal{L}_\infty$ by (57). Since $\widehat{\boldsymbol{\Theta}} \in \mathcal{L}_\infty$ by (59), $\bar{\boldsymbol{u}}_{\boldsymbol{d}} \in \mathcal{L}_\infty$, and $\boldsymbol{\chi} \in \mathcal{L}_\infty$ by Assumption 7, therefore $Y \in \mathcal{L}_\infty$ using (56). ■

6. Simulation Results

The simulations presented in this section are performed using the 4th order Runge-Kutta fixed-step algorithm to propagate the orbital and attitude dynamics. The first simulation, in Subsection 6.1, illustrates the performance of the controller when required to achieve a fixed orientation relative to the orbital frame (regulation maneuver). The second simulation, in Subsection 6.2, presents the result obtained using the controller to track a time-varying reference relative to the orbital frame (tracking maneuver). Effects of aerodynamic drag and lift, gravity gradient torque and J_2 perturbation are included in the spacecraft dynamics. The NRLMSISE-00 atmospheric model is used as the true (unknown for the controller) atmospheric density. The control law in (57) is computed every 30 seconds to allow finding a suitable set of DMD surfaces lengths through the formulation of a constrained function minimization problem that minimizes $\|\boldsymbol{\chi}\|$, and includes the physical length constraints of the DMD surfaces. The MATLAB *fmincon* command is used to solve the minimization problem

$$\min_{L_1,L_2,L_3,L_4} \|Y\widehat{\boldsymbol{\Theta}} - \bar{\boldsymbol{u}}_{\boldsymbol{d}}\| \quad \text{subject to} \quad \begin{cases} 0 \le L_j \le 3.7, \quad j = 1,2,3,4. \end{cases} \tag{75}$$

The spacecraft is simulated in a circular orbit with inclination of 51.94 degrees and 400 km altitude, similar to that of the International Space Station (ISS). The initial orbital elements and spacecraft parameters are presented in Tables 1 and 2, respectively. Additionally, the simulations also incorporate modeling inaccuracies in the CoM location and inertia matrix. For visualization purposes, in the subsequent simulation results, the orientation of the body with respect to the orbital frame is expressed using a 3-2-1 Euler angle sequence, where ϕ, θ and ψ denote the roll, pitch and yaw angles, respectively (see [17] for details). The roll, pitch and yaw angles correspond to rotations about $\hat{\boldsymbol{b}}_{\mathbf{1}}$, $\hat{\boldsymbol{b}}_{\mathbf{2}}$ and $\hat{\boldsymbol{b}}_{\mathbf{3}}$, respectively. Simulation parameters, initial conditions and uncertainties are the same for both simulation examples. The initial conditions (ϕ_0, θ_0, ψ_0) are presented in Table 3.

Parameter	Value
Semi-Major Axis $[m]$	6778×10^3
Eccentricity	0
Inclination $[deg]$	51.94
RAAN $[deg]$	206.26
Arg. of Perigee $[deg]$	101.07
True Anomaly $[deg]$	108.08

Table 1: Initial orbital parameters for simulation of regulation and tracking maneuvers.

Parameter	Value
CubeSat Body Mass $[kg]$	3
DMD Surface Mass $[kg]$	9×10^{-2}
Max. DMD Surface Length $[m]$	3.7
DMD Surface Width $[m]$	3.8×10^{-2}

Table 2: Spacecraft parameters for simulation of regulation and tracking maneuvers.

Parameter	Value
ϕ_0 $[deg]$	45
θ_0 $[deg]$	-60
ψ_0 $[deg]$	50
$\dot{\phi}_0$ $[deg/s]$	5×10^{-2}
$\dot{\theta}_0$ $[deg/s]$	-7.5×10^{-2}
$\dot{\psi}_0$ $[deg/s]$	6×10^{-2}

Table 3: Initial Euler angles and angle rates for simulation of regulation and tracking maneuvers.

6.1. Regulation Maneuver

To propagate the spacecraft dynamics, a model to compute the inertia matrix J_m as function of the DMD-surfaces lengths is used. Specifically, J_m is computed by representing a 2U CubeSat structure as a rectangular box, and the rolled and deployed portions of a DMD-surface are modeled as a thick walled cylinder and a flat plate, respectively. The inaccuracy of J_m is introduced by incorporating deviations in the mass for each part of the spacecraft and the assumed locations of their individual CoMs are shown in Table 4.

Parameter	Real (for J)	Approx. (for J_m)
CoM CubeSat Body [cm]	$[0\ 0\ 0]^T$	$[1.8\ 2\ -3]^T$
CoM Flat Plate $(\times 10^{-2})$ [m]	$[0\ 0\ 0]^T$	$[4.5L_j^2\ 0\ 0]^T$
Deployer mass [g]	89.88	75

Table 4: Uncertainties included in simulation to compute J_m. CoMs expressed in coordinate systems centered at the geometric center of the body of interest, where $j = 1,\ 2,\ 3,\ 4$.

The objective for this maneuver is to achieve a fixed orientation of the spacecraft with respect to the orbital frame. The controller parameters are shown in Table 5, and the desired Euler angles are presented in Table 6. Figures 3 and 4 show the resulting quaternion error components and the corresponding transformation to Euler angles for a 10 hour simulation, respectively. The results show that the regulation objective was achieved with ultimate bounds for roll, pitch and yaw within ± 3, ± 2 and ± 2.2 degrees, respectively.

As concluded in the stability analysis, the resulting ultimate bound can be attributed to the size of the disturbance torques in $\boldsymbol{\delta}$, the residual error $\boldsymbol{\chi}$, the unmodeled effects of the DMD on the inertia matrix, and the rate of change of the uncertain parameters (i.e., $\dot{\boldsymbol{\Theta}}$). Therefore, efforts on improving the knowledge of the inertia matrix, using a good numerical algorithm to solve for the lengths and avoiding high deployment rates, would have direct influence on reducing the ultimate bounds.

The levels of deployment for the DMD surfaces are shown in Figure 5. Actuator saturation was applied to account for the physical limits of the DMD surfaces. Although this saturation was not explicitly modeled in the controller design, the controller has shown to be robust enough to regulate the orientation despite the physical actuator limits. In an effort to reduce the influence of rapid variations of the control inputs, a low-pass filter with cutoff frequency $\omega_c \triangleq 0.017$ Hz has been applied to the lengths calculated by the *fmincon* algorithm and the maximum deployment rate among all DMD surfaces for this maneuver was 2.9 meters per minute. The norm of the resulting mismatch between $\bar{\boldsymbol{u}}$ and $\bar{\boldsymbol{u}}_{\boldsymbol{d}}$ (i.e., $\|\boldsymbol{\chi}\|$) is shown in Figure 6. Due to the amplitude limitations of the environmental torques, the actuators reached their saturation limits multiple times during approximately the first five hours of the maneuver. However, after the period of saturation, $\|\boldsymbol{\chi}\|$ remained below 1×10^{-6} Nm.

The estimated parameters in $\widehat{\boldsymbol{\Theta}}$ are shown in Figures 7 and 8 for the parameters associated with the aerodynamic drag and in Figures 9 and 10 for the parameters associated with the aerodynamic lift. The estimations are divided into four plots to better observe their variation over time because of their different orders of magnitude. From the stability analysis, it cannot be concluded that the estimation error $\widetilde{\boldsymbol{\Theta}}$ converges to zero, meaning that there is no on-line parameter estimation. However, the results show that all parameters are dynamically adjusted to compensate for the environmental and physical uncertainties and remain bounded.

Parameter	Value
$K_1\ (\times 10^{-3})$	$\mathrm{diag}(3,3,3)$
$\beta\ \left(\times 10^{-3}\right)$	$\mathrm{diag}(1.5,5,5)$
$\beta_1\ \left(\times 10^{-6}\right)$	3.2
Γ	$\mathrm{diag}\left(\Gamma_2,\Gamma_2,\Gamma_2,\Gamma_2,6\Gamma_2,6\Gamma_2,\Gamma_1,\Gamma_1,10^{-20}\right)$
$\Gamma_1\ \left(\times 10^{-19}\right)$	$\mathrm{diag}\left(1,10^{11},1,10^{11},1,10^{11},1,10^{11}\right)$
$\Gamma_2\ \left(\times 10^{-22}\right)$	$\mathrm{diag}\left(2,2^{11},2,2^{11},2,2^{11},2,2^{11}\right)$

Table 5: Controller parameters used for simulation of regulation and tracking maneuvers.

$\phi_d\ [deg]$	$\theta_d\ [deg]$	$\psi_d\ [deg]$
45	0	10

Table 6: Desired orientation of the spacecraft with respect to the orbital frame for the regulation maneuver.

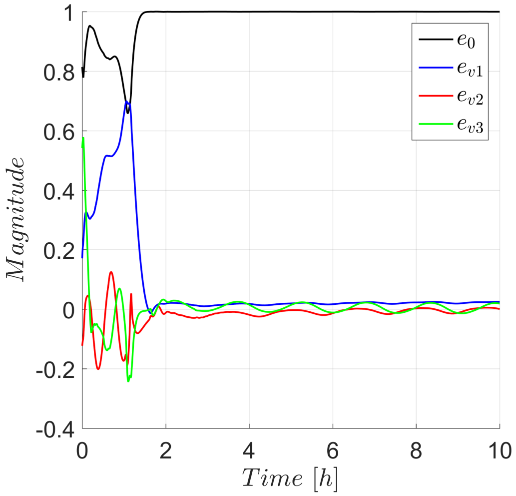

Figure 3: Resulting error quaternion for the regulation maneuver using the designed controller.

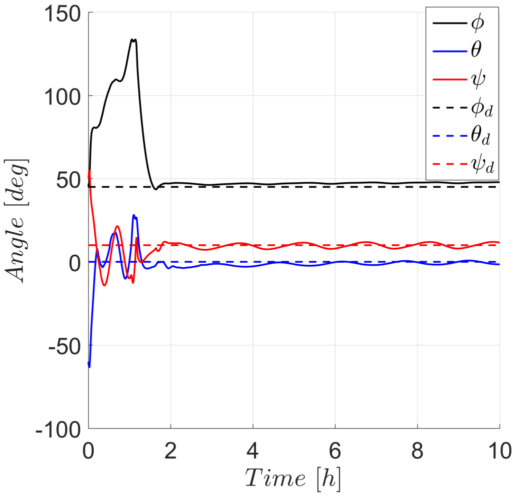

Figure 4: Resulting Euler angles for the regulation maneuver using the designed controller.

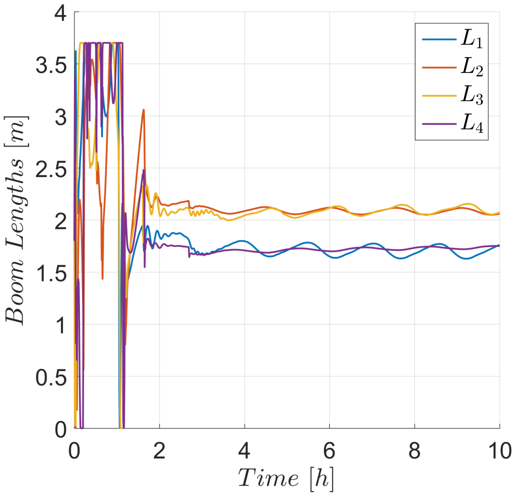

Figure 5: Required level of deployment for the DMD surfaces using the designed controller for the regulation maneuver.

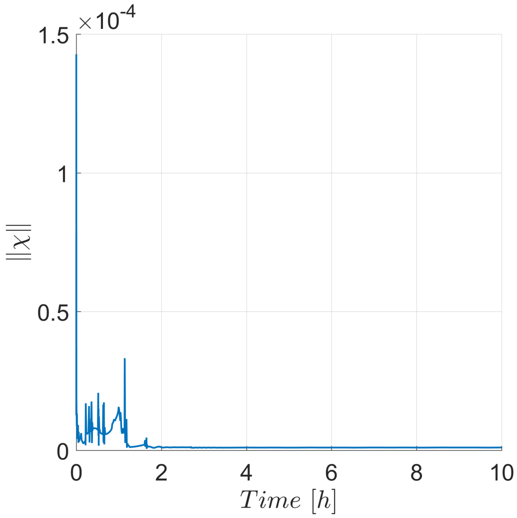

Figure 6: Resulting mismatch $\|\boldsymbol{\chi}\|$ obtained using MATLAB *fmincon* to solve for the DMD surfaces lengths for the regulation maneuver.

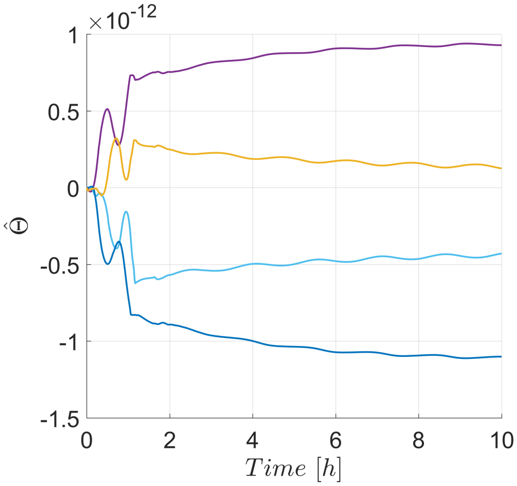

Figure 7: Resulting parameter estimates $\widehat{B}_1\widehat{C}_{D,j}$ in $\widehat{\boldsymbol{\Theta}}$ with $j = 1, 2, 3, 4$ associated with the aerodynamic drag for the regulation maneuver using the designed controller.

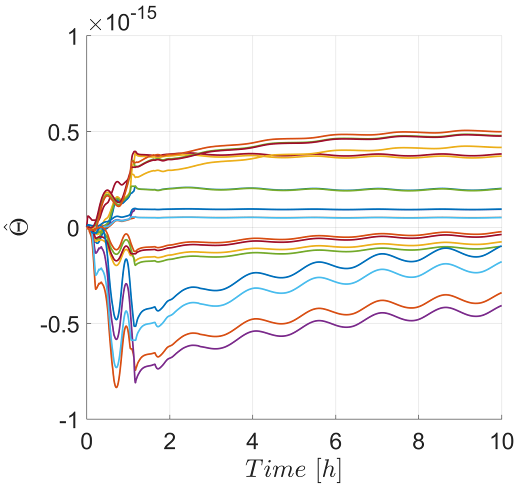

Figure 8: Resulting parameter estimates $\left[\hat{c}_1\widehat{B}_1\widehat{C}_{D,j},\ \hat{c}_1\widehat{B}_2\widehat{C}_{D,j},\ \hat{c}_2\widehat{B}_1\widehat{C}_{D,j},\ \hat{c}_2\widehat{B}_2\widehat{C}_{D,j},\ \hat{c}_3\widehat{B}_1\widehat{C}_{D,j},\ \hat{c}_3\widehat{B}_2\widehat{C}_{D,j}\right]^T$ in $\widehat{\boldsymbol{\Theta}}$ with $j = 1, 2, 3, 4$ associated with the aerodynamic drag for the regulation maneuver using the designed controller.

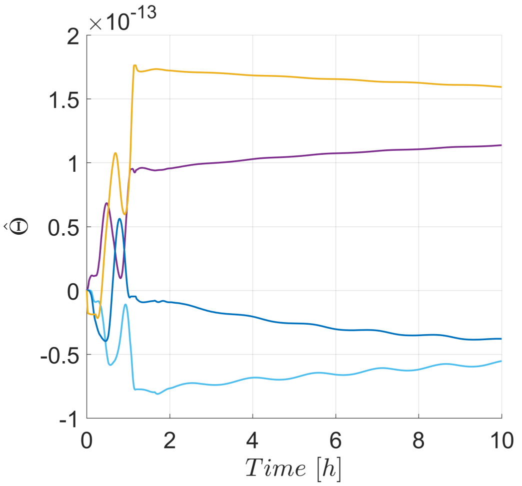

Figure 9: Resulting parameter estimates $\widehat{B}_1\widehat{C}_{L,j}$ in $\widehat{\boldsymbol{\Theta}}$ with $j = 1, 2, 3, 4$ associated with the aerodynamic lift for the regulation maneuver using the designed controller.

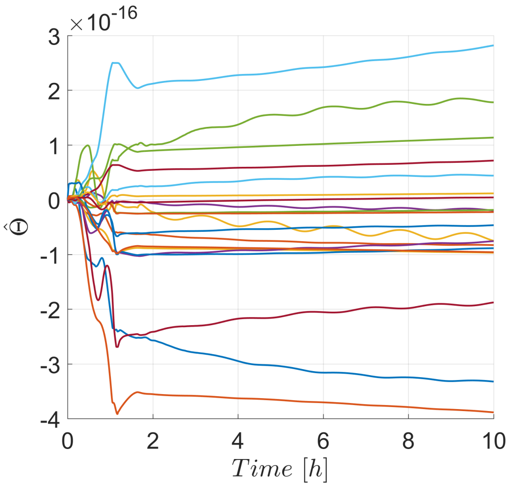

Figure 10: Resulting parameter estimates $\left[\hat{c}_1\widehat{B}_1\widehat{C}_{L,j},\ \hat{c}_1\widehat{B}_2\widehat{C}_{L,j},\ \hat{c}_2\widehat{B}_1\widehat{C}_{L,j},\ \hat{c}_2\widehat{B}_2\widehat{C}_{L,j},\ \hat{c}_3\widehat{B}_1\widehat{C}_{L,j},\ \hat{c}_3\widehat{B}_2\widehat{C}_{L,j}\right]^T$ in $\widehat{\boldsymbol{\Theta}}$ with $j = 1, 2, 3, 4$ associated with the aerodynamic lift for the regulation maneuver using the designed controller.

For the specific spacecraft and orbit considered in the regulation example, a feasible range of operation including saturation of the control inputs is determined by performing a set of 1000 five-hour simulations of regulation maneuvers. The initial conditions and the desired Euler angles are randomly initialized as shown in Table 7. The set of possible desired Euler angles has been selected so that the operational range for a more demanding mission as compared to the previous example is considered (e.g., pointing a camera on the ram/anti-ram face of the spacecraft to a given objective).

To point the $\hat{\boldsymbol{b}}_{\boldsymbol{1}}$ body axis towards any direction inside a cone of limited size with respect to the along-track direction $\hat{\boldsymbol{o}}_{\boldsymbol{1}}$, it is sufficient to vary the desired roll and yaw angles. The size of the cone is driven by the bounds of the yaw angle and all directions inside the cone are explored by varying the roll angle. For all simulations, the spacecraft is considered stabilized if $\|\boldsymbol{e_v}\| \leq 0.4$ (user-defined) on average during the last 20 minutes of the maneuver, which was found representative for successful maneuvers considering the ultimately bounded result from the stability analysis. Figure 11 presents the percentage of stabilized maneuvers with different limits for the norm of the yaw angle $\|\psi\|$ (i.e., cone sizes). Figure 12 illustrates the difference in size between cones resulting from yaw bounds of ±8 and ±25 degrees, with percentages of success of 80% and 70%, respectively. The remaining percentage of failure can be attributed to several factors including the limitations due to the DMD geometry, initial conditions, and variations of atmospheric density, among others.

Parameter	Range
$\phi_0,\ \theta_0,\ \psi_0$ [deg]	$[-10, 10]$
$\dot{\phi}_0,\ \dot{\theta}_0,\ \dot{\psi}_0$ [deg/s]	$[-0.02, 0.02]$
ϕ_d [deg]	$[-180, 180]$
θ_d [deg]	0
ψ_d [deg]	$[-25, 25]$

Table 7: Parameter ranges for the set of 1000 five-hour simulations.

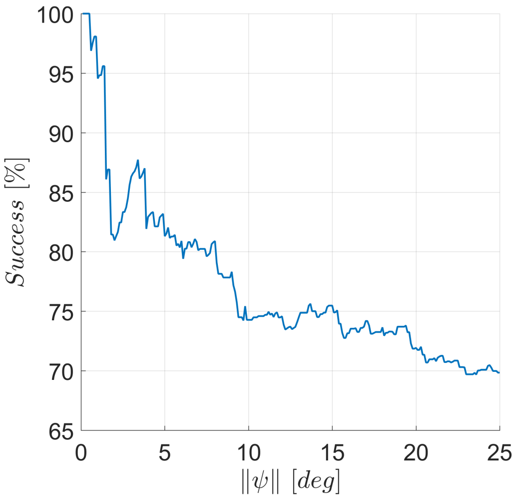

Figure 11: Resulting percentage of successful regulation maneuvers vs. size of the cone.

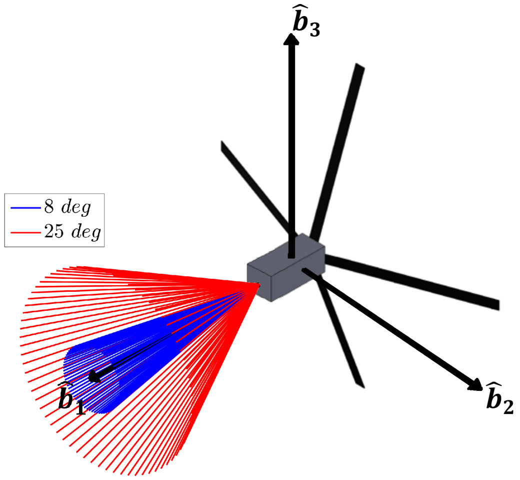

Figure 12: Resulting feasible range of operation, 8 degrees (80%), 25 degrees (70%).

6.2. Tracking Maneuver

The simulation presented in this subsection illustrates a scenario where the CubeSat is required to change its orientation with respect to the orbital frame over time. This task could be required for missions where the spacecraft needs to adjust its orientation for pointing a sensor (e.g., a camera) towards different areas during the mission. The scenario considers a spacecraft that is required to track a desired trajectory of the roll angle while keeping the pitch and yaw angles fixed. The initial conditions and control parameters are the same used for the regulation maneuver, and the desired Euler angles are presented in Table 8.

Figures 13 and 14 show the resulting quaternion error components and the corresponding transformation to Euler angles for a 10 hour simulation. These results show that the CubeSat orientation reaches the ultimate bound in approximately 5 hours. The ultimate bounds for roll, pitch and yaw are ± 3, ± 1.5 and ± 3 degrees, respectively.

The resulting lengths of the DMD are shown in Figure 15, where saturation to account for the physical constraints was applied. The DMD surfaces reached their saturation levels multiple times during the first two hours of the simulation, and the controller has shown to be robust during that portion of the maneuver. The maximum deployment rate among all DMD surfaces for the tracking maneuver was 2.6 meters per minute. Figure 16 shows the norm of the mismatch between $\bar{\boldsymbol{u}}$ and $\bar{\boldsymbol{u}}_{\boldsymbol{d}}$ (i.e., $\|\boldsymbol{\chi}\|$), after the period of saturation, it remained below 8.9×10^{-7} Nm.

The estimated parameters in $\widehat{\boldsymbol{\Theta}}$ are shown in Figures 17 and 18 for parameters associated with the aerodynamic drag and in Figures 19 and 20 for those associated with the aerodynamic lift. All the estimations remain bounded and are dynamically adjusted to compensate for the uncertainties but on-line estimation cannot be guaranteed.

ϕ_d $[deg]$	θ_d $[deg]$	ψ_d $[deg]$
$35 + 15\sin(4.36 \times 10^{-4}t)$	0	0

Table 8: Desired orientation of the spacecraft with respect to the orbital frame for the tracking maneuver.

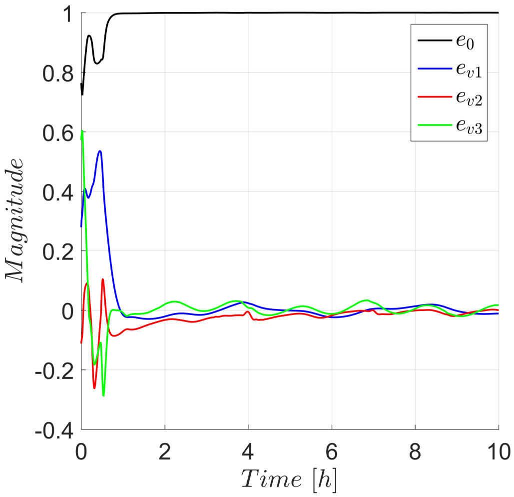

Figure 13: Resulting error quaternion for the tracking maneuver using the designed controller.

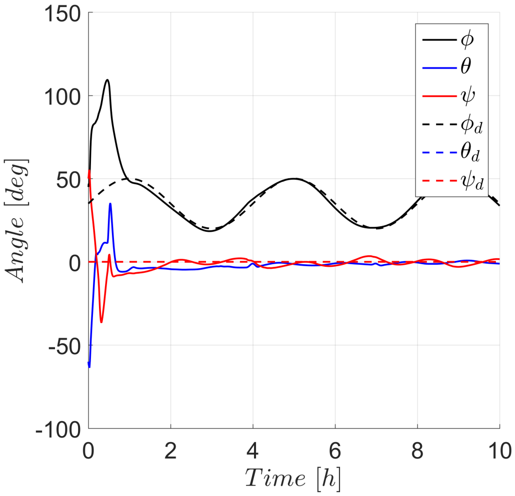

Figure 14: Resulting Euler angles for the tracking maneuver using the designed controller.

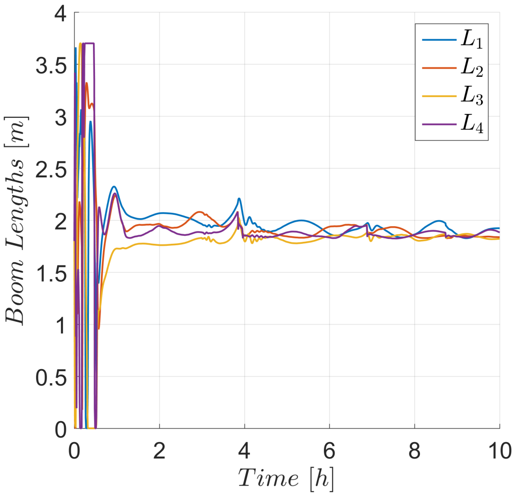

Figure 15: Required level of deployment for the DMD surfaces using the designed controller for the tracking maneuver.

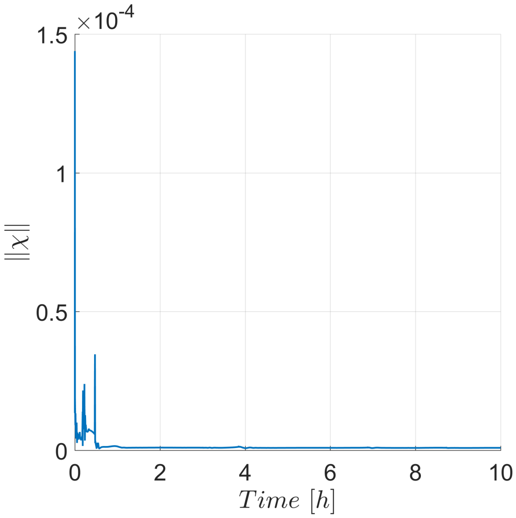

Figure 16: Resulting mismatch $\|\boldsymbol{\chi}\|$ obtained using MATLAB *fmincon* to solve for the DMD surfaces lengths for the tracking maneuver.

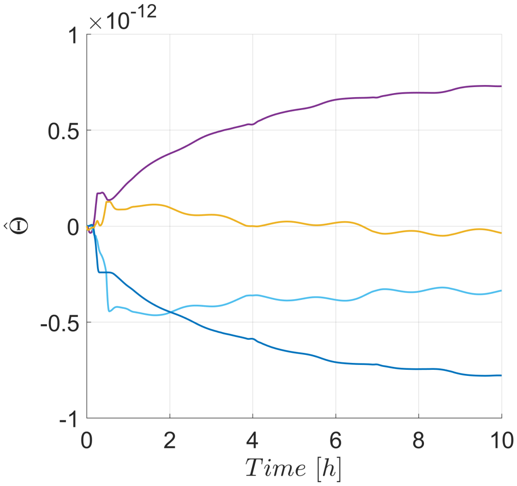

Figure 17: Resulting parameter estimates $\widehat{B}_1\widehat{C}_{D,j}$ in $\widehat{\boldsymbol{\Theta}}$ with $j = 1, 2, 3, 4$ associated with the aerodynamic drag for the tracking maneuver using the designed controller.

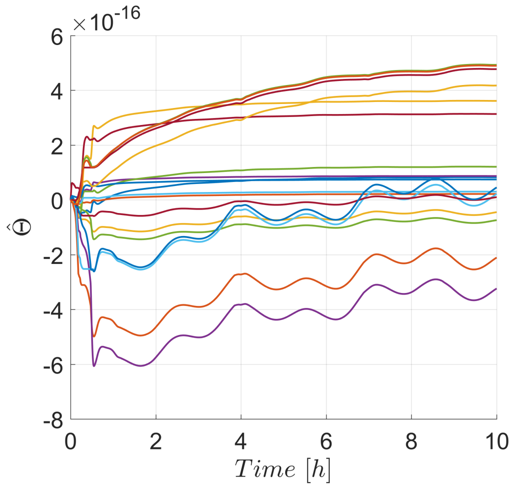

Figure 18: Resulting parameter estimates $\left[\hat{c}_1\widehat{B}_1\widehat{C}_{D,j},\ \hat{c}_1\widehat{B}_2\widehat{C}_{D,j},\ \hat{c}_2\widehat{B}_1\widehat{C}_{D,j},\ \hat{c}_2\widehat{B}_2\widehat{C}_{D,j},\ \hat{c}_3\widehat{B}_1\widehat{C}_{D,j},\ \hat{c}_3\widehat{B}_2\widehat{C}_{D,j}\right]^T$ in $\widehat{\mathbf{\Theta}}$ with $j = 1, 2, 3, 4$ associated with the aerodynamic drag for the tracking maneuver using the designed controller.

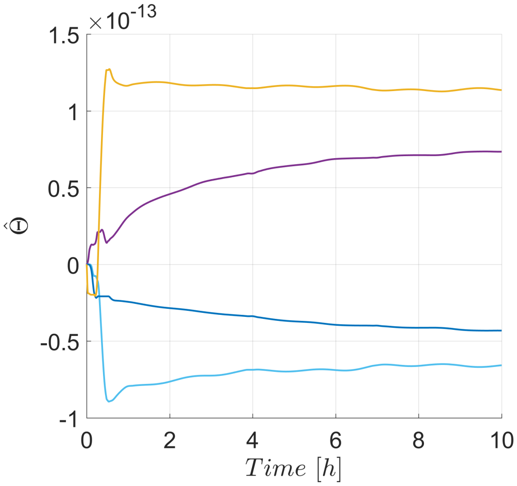

Figure 19: Resulting parameter estimates $\widehat{B}_1\widehat{C}_{L,j}$ in $\widehat{\mathbf{\Theta}}$ with $j = 1, 2, 3, 4$ associated with the aerodynamic lift for the tracking maneuver using the designed controller.

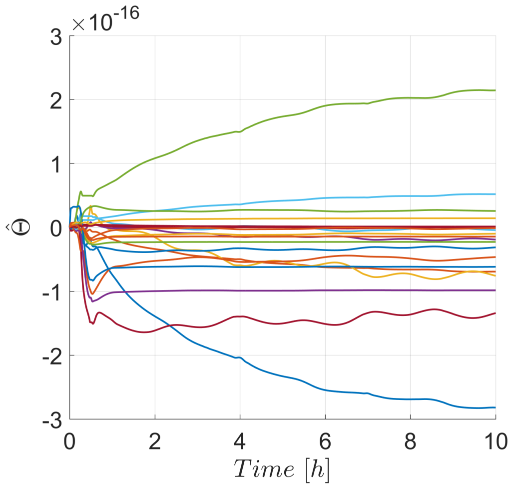

Figure 20: Resulting parameter estimates $\left[\hat{c}_1\widehat{B}_1\widehat{C}_{L,j},\ \hat{c}_1\widehat{B}_2\widehat{C}_{L,j},\ \hat{c}_2\widehat{B}_1\widehat{C}_{L,j},\ \hat{c}_2\widehat{B}_2\widehat{C}_{L,j},\ \hat{c}_3\widehat{B}_1\widehat{C}_{L,j},\ \hat{c}_3\widehat{B}_2\widehat{C}_{L,j}\right]^T$ in $\widehat{\boldsymbol{\Theta}}$ with $j = 1, 2, 3, 4$ associated with the aerodynamic lift for the tracking maneuver using the designed controller.

To illustrate the approach taken to evaluate the effect that the applied torques may have on the long DMD surfaces, a comparison between the frequency content of the applied torque and the first natural frequencies of a DMD surface was performed for the tracking maneuver. A fully deployed DMD surface was modeled as a cantilevered beam and the first natural frequencies were computed using SolidWorks. Figure 21 illustrates the first five mode shapes and their corresponding frequencies, and Figure 22 shows the Fast Fourier Transform (FFT) of each component of the applied torque. From these figures, the range of frequencies of the applied torques is reasonably below the first natural frequency of the DMD surface (i.e., 0.1396 Hz).

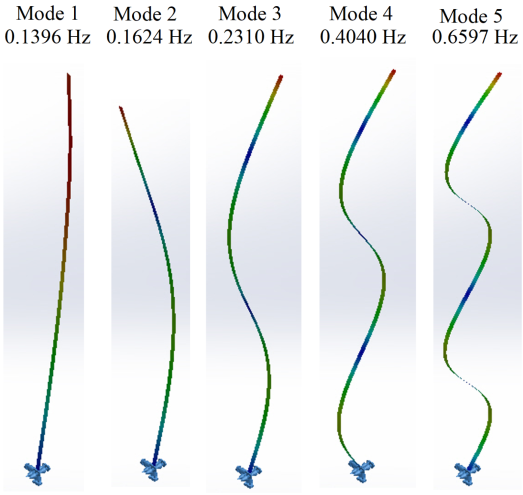

Figure 21: First natural frequencies of a fully deployed DMD surface.

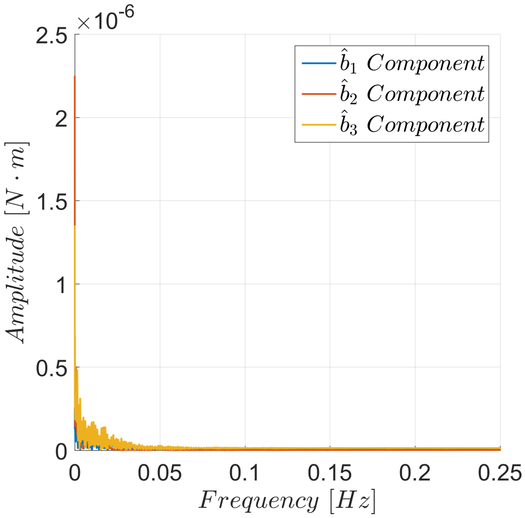

Figure 22: FFT of the torque $Y\widehat{\mathbf{\Theta}}$ applied during the tracking maneuver.

7. Conclusion

This paper presented the design and validation through numerical simulation of an adaptive controller for environmental torques-based attitude control that compensates for uncertainties in the atmospheric density, drag and lift coefficients, and center of mass location. Moreover, the controller also considers perturbations associated with the non-modeled behavior of the inertia matrix. The obtained result ensures the alignment of the body and orbital frames within ultimate bounds. Simulation results including aerodynamic and gravity gradient torques, actuator saturation, as well as the NRLMSISE-00 model for atmospheric density and J_2 perturbation, were performed to validate regulation and tracking of the angles to their desired values relative to the orbital frame within bounds of ± 3 deg. Therefore, the controller shows potential for applications where the location of the center of mass, atmospheric density, drag coefficients are uncertain and the inertia matrix cannot be accurately computed in real time. Future work on this problem will consider strategies to address implementation challenges such as failures to deploy a DMD surface.

Acknowledgments

This research has been supported by the Fulbright Colombia Commission and the AFOSR award number FA9550-19-1-0169. Any opinions, findings and conclusions or recommendations expressed in this material are those of the authors and do not necessarily reflect the views of the sponsoring agency.

References

[1] T. C. Program, Cubesat design specification rev.13 (2015).

[2] M. I. Martinelli, R. S. Sanchez-Peña, Passive 3 axis attitude control of msu-1 pico-satellite, Acta Astronautica 56 (2005) 507–517. `doi:10.1016/j.actaastro.2004.10.007`.

[3] M. Pastorelli, R. Bevilacqua, S. Partorelli, Differential-drag-based roto-translational control for propellant-less spacecraft, Acta Astronautica 114 (2015) 6–21. `doi:j.actaastro.2015.04.014`.

[4] R. Sun, J. Wang, D. Zhang, Q. Jia, X. Shao, Roto-translational spacecraft formation control using aerodynamic forces, Journal of Guidance, Control and Dynamics 40 (10) (2017) 2556–2568. `doi:10.2514/1.G003130`.

[5] R. Sutherland, I. Kolmanovsky, A. R. Girard, Attitude control of a 2u cubesat by magnetic and air drag torques, IEEE Transactions on Control Systems Technology 27 (3) (2019) 1047–1059. `doi:10.1109/TCST.2018.2791979`.

[6] A. Harris, C. D. Petersen, H. Schaub, Linear coupled attitude-orbit control through aerodynamic forces, AIAA Journal of Guidance, Control and Dynamics 43 (1) (2020) 122–131. `doi:10.2514/1.G004521`.

[7] C. L. Leonard, M. Hollister, E. V. Bergman, Orbital formationkeeping with differential drag, Journal of Guidance, Control and Dynamics 12 (1) (1989) 108–113. `doi:10.2514/3.20374`.

[8] R. Bevilacqua, M. Romano, Rendezvous maneuvers of multiple spacecraft by differential drag under j2 perturbation, Journal of Guidance, Control and Dynamics 31 (6) (2008) 1595–1607. `doi:10.2514/1.36362`.

[9] M. Horsley, S. Nikolaev, A. Pertica, Rendezvous maneuvers of small spacecraft using differential lift and drag, Journal of Guidance, Control and Dynamics 36 (2) (2011) 445–453. `doi:10.2514/1.57327`.

[10] R. Perez, D. an Bevilacqua, Differential drag spacecraft rendezvous using an adaptive lyapunov control strategy, Acta Astronautica 83 (2013) 196–207. `doi:10.1016/j.actaastro.2012.09.005`.

[11] D. Ivanov, M. Kushniruk, M. Ovchinnikov, Study of satellite formation flying control usign differential lift and drag, Acta Astronautica 152 (2018) 88–100. `doi:10.1016/j.actaastro.2018.07.047`.

[12] D. Guglielmo, S. Omar, R. Bevilacqua, L. Fineberg, J. Treptow, B. Poffenberger, Y. Johnson, Drag de-orbit device: A new standard reentry actua-

tor for cubesats, Journal of Spacecraft and Rockets 56 (1) (2018) 129–145. `doi:10.2514/1.A34218`.

[13] S. Omar, D. Guglielmo, R. Bevilacqua, Drag de-orbit device (d3) mission for validation of controlled spacecraft re-entry using aerodynamic drag, in: 4th IAA Dynamics and Control of Space Systems Conference, Rome, Italy., 2017.

[14] S. Omar, R. Bevilacqua, Hardware and GNC solutions for controlled spacecraft re-entry using aerodynamic drag, Acta Astronautica 159 (2019) 49–64. `doi:j.actaastro.2019.03.051`.

[15] C. Riano-Rios, R. Bevilacqua, W. E. Dixon, Adaptive control for differential drag-based rendezvous maneuvers with an unknown target, Acta Astronautica, In Press. `doi:j.actaastro.2020.03.011`.

[16] C. Riano-Rios, R. Bevilacqua, W. E. Dixon, Differential drag-based multiple spacecraft maneuvering and on-line parameter estimation using integral concurrent learning, Acta Astronautica 174 (2020) 189–203. `doi:j.actaastro.2020.04.059`.

[17] C. Riano-Rios, S. Omar, R. Bevilacqua, W. E. Dixon, Spacecraft attitude regulation in low earth orbit using natural torques, in: 2019 IEEE 4th Colombian Conference on Automatic Control (CCAC), Medellin, Colombia., 2019.

[18] S. Omar, C. Riano-Rios, R. Bevilacqua, Semi-passive three axis attitude stabilization for earth observation satellites using the drag maneuvering device, in: 12th Symposium on Small Satellite for Earth Observation. Berlin, Germany, 2019.

[19] R. Sun, C. Riano-Rios, R. Bevilacqua, N. G. Fitz-Coy, W. E. Dixon, Cubesat adaptive attitude control with uncertain drag coefficient and atmospheric density, AIAA Journal of Guidance, Control and Dynamics, to appear.

[20] J. Virgili-Llop, H. C. Polat, M. Romano, Attitude stabilization of spacecraft in very low earth orbit by center-of-mass shifting, Frontiers in Robotics and AI 6 (2019) 1–9. `doi:https://doi.org/10.3389/frobt.2019.00007`.

[21] I. Palunko, R. Fierro, Adaptive control of a quadrotor with dynamic changes in the center of gravity, in: Proceedings of the 18th IFAC World Congress, Milano, Italy., 2011.

[22] D. Thakur, S. Srikant, M. R. Akella, Adaptive attitude-tracking control of spacecraft with uncertain time-varying inertia parameters, Journal of Guidance, Control, and Dynamics 38 (1) (2015) 41–52. `doi:10.2514/1.G000457`.

[23] J. R. Wertz, D. F. Everett, J. Puschell, Space mission engineering: the new SMAD, 3rd Edition, Microcosm Press, 2011.

[24] E. P. Blackburn, D. DeBra, D. Dobrotin, J. Scull, R. E. Fischell, D. Fosth, J. Kelly, A. J. Fleig, H. Perkel, R. E. Roberson, J. Rodden, B. Tinling, S. O'Neil, F. J. Carroll, R. F. Bohling, NASA space vehicle design criteria monograph (guidance and control), NASA SP-8018.

[25] P. Hughes, Spacecraft Attitude Dynamics, Dover Books on Aeronautical Engineering, Dover Publications, 2012.

[26] NOAA, U.S. standard atmosphere (1976).

[27] I. Harris, W. Priester, Time-dependent structure of the upper atmosphere, Journal of the Atmospheric Sciences 19 (4) (1962) 286–301. `doi:10.1175/1520-0469(1962)019<0286:TDSOTU>2.0.CO;2`.

[28] J. M. Picone, A. E. Hedin, D. P. Drob, A. C. Aikin, Nrlmsise-00 empirical model of the atmosphere: Statistical comparisons and cientific issues, Journal of Geophysical Research 107 (A12) (2002) 15–1–15–16. `doi:10.1029/2002JA009430`.

[29] O. Montenbruck, E. Gill, Satellite Orbits: Models, Methods and Applications, Springer, Berlin, 2000.

[30] M. Pilinski, Dynamic gas-surface interaction modeling for satellite aerodynamic computations, Ph.D. thesis, University of Colorado Boulder (2011).

[31] C. W. Hall, Laws and Models: Science, Engineering and Technology, 1st Edition, CRC PRess, 2018.

[32] H. Schaub, J. L. Junkins, Analytical Mechanics of Space Systems, AIAA Education Series, Reston, VA, 2014. `doi:10.2514/4.105210`.

[33] Z. Cai, M. S. de Queiroz, D. M. Dawson, A sufficiently smooth projection operator, IEEE Transactions on Automatic Control 51 (1) (2006) 135–139. `doi:10.1109/TAC.2005.861704`.

[34] H. K. Khalil, Nonlinear Systems, 3rd Edition, Prentice Hall, NJ, 2002.